Received: 24 March 2025 | Revised: 7 November 2025 | Accepted: 13 November 2025

DOI: 10.1002/qj.70084

Quarterly Journal of the Royal Meteorological Society RMetS

RESEARCH ARTICLE

# Dynamics and model representation of two contrasting extreme precipitation events in the Sahel

**Souleymane Sanogo**[1] | **Marlon Maranan**[2] | **Andreas H. Fink**[2] | **Beth J. Woodhams**[2] | **Peter Knippertz**[2]

[1]Faculté des Sciences et Techniques (FST), Université des Sciences des Techniques et de Technologie de Bamako (USTT-B), Bamako, Mali

[2]Institute of Meteorology and Climate Research (IMKTRO), Karlsruhe Institute of Technology (KIT), Karlsruhe, Germany

**Correspondence**
Marlon Maranan, Institute of Meteorology and Climate Research (IMKTRO), Karlsruhe Institute of Technology (KIT), Karlsruhe, Germany.
Email: marlon.maranan@kit.edu

**Funding information**
German Federal Ministry of Education and Research (BMBF) through the WASCALResearch Action Plan 2.0 (WRAP2.0) for FURIFLOOD project (Current and future risks of urban and rural f looding in West Africa- An integrated analysis and eco-system-based solutions; grant No. 01LG2086A) and also from the BMBFproject NetCDA (German Academic Network for Capacity Development in Climate Change Adaptations in Africa; grant No. 01LG2301E); Deutsche Forschungsgemeinschaft (grant no. SFB/TRR 165, "Waves to Weather") and conducted within the subproject C2: "Statistical-dynamical forecasts of tropical rainfall"; DAAD Climate Research Alumni and Postdocs in Africa-(climapAfrica) Programme.

## Abstract

Two extreme flood-inducing precipitation events in two cities in Mali, on August 8, 2012 in San (127 mm) and on August 25, 2019 in Kenieba (126 mm), are investigated with respect to rainfall structures, dynamical forcings, and the ability of the ICOsahedral Nonhydrostatic model (ICON) to represent their evolution. Two sets of experiments with convective parameterization enabled (PARAM) and disabled (EXPLC), both at 6.5-km grid spacing, are conducted for each case. While the (thermo)dynamical fields of the simulations are compared with fifth-generation European Centre for Medium-Range Weather Forecasts (ECMWF) reanalysis (ERA5) data, the rainfall fields are tested against the satellite-based precipitation dataset Integrated Multi-satellitE Retrievals for *Global Precipitation Measurement* (*GPM*) (IMERG) by applying spatial verification methods based on the fractions skill score (FSS) and structure–amplitude–location (SAL) score. In addition, a spectral filtering of tropical waves is applied to investigate their impact on extreme events. The most prominent results are as follows. (1) Both cases were caused by organized convective systems associated with a westward-propagating cyclonic vortex, but differ in their environmental setting. Although both cases featured an African easterly wave, the San case involved convective enhancement along dry Saharan airmasses, whereas the Kenieba case occurred within an unusual widespread wet environment extending deep into the Sahel. (2) Although EXPLC captures the rainfall distribution in the San case better than PARAM, it fails to organize convection in the moisture-laden Kenieba case, which PARAM is capable of simulating. (3) The FSS confirms the case dependence of the ICON skill. The SAL method hints at a systematic deficiency of EXPLC in representing convective organization by producing too many scattered and weak rainfall systems, while PARAM is more effective in converting abundant moisture into excessive rainfall. The results stress the continued need for more research into capturing the complex convective dynamics to forecast the extremes of Sahelian rainfall better.

**KEYWORDS**

convection, extreme precipitation, ICON model, monsoon, Sahel, spatial verification, West Africa

## 1 | INTRODUCTION

While the semi-arid zone of West Africa suffered enormously under the great droughts of the 1980s, the rainfall recovery since the 1990s has been associated with frequent episodes of intense rainfall (Nicholson *et al.*, 2018; Panthou *et al.*, 2014; Sanogo *et al.*, 2015). This trend is expected to continue as the planet warms (Berthou *et al.*, 2019; Kendon *et al.*, 2019; Westra *et al.*, 2014). Indeed, the decades that followed the 1990s were marked by the occurrence of extreme precipitation events that have often led to flooding and subsequent impairment of water quality, human health, and ecosystems. Those extreme rainfall events affected urban transportation, agriculture, infrastructure, and human lives in many countries across the Sahel (Tschakert *et al.*, 2010), causing considerable socio-economic damages and losses (Douglas *et al.*, 2008). According to OCHA (2017), more than 11,000 people in Mali alone were affected by floods in the early rainy season of 2017. Pastoral communities were particularly affected, with more than 26,000 animals lost across the country. On May 16, 2019, the Malian Red Cross reported a flood event with water levels up to 2.5 m that affected the capital city Bamako, after a sudden torrential downpour lasting several hours (IFRC, 2019). Such extreme events need to be understood better in order to improve forecast and warning systems, which, crucially, could prevent damage and minimize risks.

The West African monsoon constitutes a dominating atmospheric feature controlling the large-scale circulation and local precipitation over West Africa. In this regional system, a southwesterly flow is formed between the Gulf of Guinea and the Saharan Heat Low (SHL), which brings moisture to the continent (Knippertz *et al.*, 2017; Raji *et al.*, 2017; Thorncroft *et al.*, 2011). This mechanism provides the conditions for precipitation in the Sahel from May–October. Many West African rainy seasons in recent decades have been harsh, due to the frequent occurrence of flood-inducing rains (Atiah *et al.*, 2023; Engel *et al.*, 2017; Fall *et al.*, 2020; Nicholson *et al.*, 2022; Njau & Thiaw, 2011; Paeth *et al.*, 2011; Sima *et al.*, 2013). Some events have attracted the attention of the scientific community, in particular the cases of September 1, 2009 in Ouagadogou, Burkina Faso (Beucher *et al.*, 2020; Engel *et al.*, 2017; Lafore *et al.*, 2017), August 26, 2012 in Dakar, Senegal (Engel *et al.*, 2017), June 12, 2016 in Abakaliki, Nigeria (Maranan *et al.*, 2019), and August 26, 2017 in Linguère, Senegal (Fall *et al.*, 2020).

The weather systems associated with rainfall events in the Sahel vary throughout the year depending on the stage of the West African monsoon (Fink *et al.*, 2006; Janiga & Thorncroft, 2014; Maranan *et al.*, 2018, 2020). While the peak monsoon period in the Sahel in July and August is dominated by highly organized mesoscale convective systems (MCSs: Fink & Reiner, 2003; Zipser *et al.*, 2006; Guichard *et al.*, 2010), often of squall-line type (Diongue *et al.*, 2002; Fink & Reiner, 2003; Redelsperger *et al.*, 2002), the transitional months May and October feature rainfall systems that are frequently influenced by tropical–extratropical interactions such as tropical plumes (Knippertz & Fink, 2008; Knippertz & Martin, 2005; Rubin *et al.*, 2007). Squall lines, dominating the Sahel during the peak monsoon period (Fink & Reiner, 2003), are fast-propagating rainfall features, which can lead to extreme wind gusts but rarely to extreme rainfall. Typically, the associated total rainfall ranges between 20 and 50 mm and hardly exceeds 100 mm (Fink *et al.*, 2017). However, recent studies have shown that extreme precipitation events over West Africa are often caused by slow-moving MCSs. Such complex systems can be sustained by strong moisture convergence within low-tropospheric vortices, sometimes related to African easterly waves (AEWs), which allow a swift moisture refueling and multiple MCS passages within a short time (Engel *et al.*, 2017; Maranan *et al.*, 2019). For example, for the extreme rainfall event in Abakaliki (Nigeria) in June 2016, such a vortex facilitated the intensification but likely also the deceleration of an MCS, which caused a transformation of the MCS from a fast Sahelian squall line into a slow-moving coastal system (Maranan *et al.*, 2019). The subsequent interaction with the vortex led to the maintenance of the MCS through constant and abundant moisture supply along the wet Guinea coast region. In a similar way, the influence of a potential AEW on moisture levels and convergence likely facilitated high precipitation rates during the Linguère case (Fall *et al.*, 2020).

The predictability of extreme rainfall in West Africa using numerical weather prediction (NWP) models has been a long-standing challenge. In general, predictions of daily rainfall occurrence over West Africa with dynamical models have low skill, often not even better than a climatological reference (Vogel *et al.*, 2020). Investigating the skill of global prediction of rainfall, Vogel *et al.* (2018) suspect that the parameterization of convection is a potential cause for the lack of ensemble forecast skill in regions such as the Sahel, which are dominated by MCSs. Pante and Knippertz (2019) used the operational weather model of the German Weather Service (Deutscher Wetterdienst, DWD), the ICOsahedral Nonhydrostatic model (ICON), to compare explicit convection with parameterized convection in simulating diurnal rainfall over the West African Sahel. Their results show that explicit convection generally leads to an improved representation of rainfall systems in the Sahel. Whether this translates to a better representation of individual extreme events in the Sahel in ICON is not well known. However, learning about the

strengths and weaknesses of state-of-the-art NWP models in these situations is crucial to identify areas for improvements and their usefulness for decision-making on an event-to-event basis. This is a key motivation for the work presented in this article.

Here, we examine two high-impact rainfall events that affected Mali during the 2012 and 2019 monsoon seasons. Between August 8 and 9, 2012, exceptionally heavy rainfall locally produced daily totals of up to 200 mm, causing extensive flooding and widespread damage to infrastructure, housing, and agriculture (Essor, 2012). Similarly, three consecutive days of intense rainfall between August 24 and 26, 2019 led to severe flooding across several regions; by August 28, the Mali Red Cross Society (MRCS) reported the destruction of 845 houses and the displacement of hundreds of people, with croplands and food stocks also heavily affected (IFRC, 2019). These two extreme events, represented in this study by rainfall observations from the Malian cities San and Kenieba, exhibit distinctly different synoptic-scale dynamics, which require an in-depth analysis of the development of their synoptic-dynamical features. Specifically, the study seeks (a) to test the capability of explicit and parameterized convection in the ICON model to simulate those rainfall systems and associated dynamic features, and (b) to identify the characteristics of the meteorological environments that favored the development of the extreme precipitation events. The latter is accompanied by investigating the potential impact of equatorial waves (Matsuno, 1966), which are known to modulate and couple with rainfall systems on synoptic time-scales (e.g., Roundy, 2018; Schlueter *et al.*, 2019a, 2019b; Wheeler & Kiladis, 1999). Furthermore, equatorial waves are related to rainfall extremes in the central Sahel (Peyrillé *et al.*, 2023) and represent a source of enhanced rainfall predictability in the Tropics (e.g., Bechtold *et al.*, 2008; Judt, 2020; Knippertz *et al.*, 2022). In the context of West Africa, investigating precipitation extremes is challenging, due to the poor availability of appropriate ground-based rainfall data, as station data are not freely accessible in most of the countries in the region and continuous daily and (sub-)hourly rainfall data for periods long enough to identify extreme rainfall events are difficult to acquire. Indeed, to conduct this study, successful efforts were made to obtain daily station rainfall data from the National Meteorological service of Mali.

The article is structured as follows: Section 2 provides information on the reference data used in this study. Section 3 describes analysis methods and model experiments. Section 4 deals with the description and examination of the environmental conditions around the extreme precipitation events on August 8, 2012 in San (referred to as the "San case" hereafter) and on August 25, 2019 in Kenieba (the "Kenieba case"). Section 5 focuses on the performance evaluation of the ICON simulations compared with observation and reanalysis data with respect to rainfall and dynamical fields. Finally, Section 6 provides a summary and conclusion.

## 2 | OBSERVATIONAL DATASETS

### 2.1 | Rain-gauges

As a reference for observed rainfall, daily rain-gauge observations are taken from long-term records (i.e., since the early 20th century) of the Karlsruhe African Surface Station Database (KASS-D: Vogel *et al.*, 2018; Schlueter *et al.*, 2019b; Seregina *et al.*, 2019). For this study, 50 stations in Mali with at least 90% of data availability in the period 1960–2019 were considered to identify extreme events, that is, daily rainfall values larger than the 95th percentile inferred from non-zero daily rainfall amounts over that same period. However, priority is given to extreme events that occurred in the period 2000–2019 to ensure the availability of Integrated Multi-satellitE Retrievals for *Global Precipitation Measurement* (*GPM*) (IMERG) data (see next subsection) for the analysis. Eventually, together with visual inspection of IMERG rainfall maps and quick-looks, the intense rainfall events at the stations San (WMO station ID 61277) and Kenieba (61285) in August 2012 and 2019, respectively, were chosen for this study.

### 2.2 | IMERG

In addition to rain-gauge records, this study uses rainfall data of IMERG (version 6B, V6B), the final run of which offered near-global data from 1998 onwards at the time of compiling this study. IMERG combines data from the era of the *Tropical Rainfall Measuring Mission* (*TRMM*, 1997–2015: Huffman *et al.*, 2007) and its successor, the *GPM* mission, launched on February 27, 2014. The *GPM* mission comprises an international constellation of satellites to provide the next generation of global observations of precipitation (Liu, 2016). Rainfall in the IMERG product is estimated by an algorithm that intercalibrates and merges precipitation estimates from the *GPM* satellite constellation of microwave sensors, microwave-calibrated infrared satellite estimates, and monthly gauge precipitation data. A decision was made against the current version 7 (V7) in response to auxiliary tests, which showed stronger underestimation tendencies of intense sub-hourly rainfall rates in V7 compared with V6B in the Guinea coast region (not shown). In any case,

the relatively fine spatial resolution of 0.1° × 0.1° and high temporal resolution of 30 min (Huffman *et al.*, 2015, 2019) makes IMERG highly relevant for investigating the evolution of extreme rainfall events. Moreover, IMERG products have shown good performance in capturing rainfall intensities in arid and semi-arid regions (Dezfuli *et al.*, 2017; Gosset *et al.*, 2018; Maranan *et al.*, 2020).

### 2.3 | ERA5

The fifth generation of the European Centre for Medium-Range Weather Forecasts (ECMWF) reanalysis (ERA5), ranging from 1940 until the present, is used for analyzing the dynamical fields associated with the selected extreme precipitation events. This global reanalysis is based on the Integrated Forecasting System (IFS) Cy41r2, which became operational in 2016 (Hersbach *et al.*, 2020). In this study, hourly data with a horizontal grid spacing of 0.25° are used. The variables of interest include relative vorticity, precipitable water, and precipitation rate. We note that ERA5 rainfall is a product of successive short-range IFS forecasts (Lavers *et al.*, 2022) and thus of the parameterization schemes in IFS.

## 3 | ANALYSIS METHODS AND MODEL EXPERIMENTS

### 3.1 | ICON model setups

ICON is a global NWP model developed jointly by DWD and the Max-Planck Institute for Meteorology in Hamburg (MPI-M: (Zängl *et al.*, 2015)). It has 90 atmospheric levels up to a maximum height of 75 km. The operational ICON setup, together with two one-way nests over West Africa, is used in this study to assess the capability of both explicit (EXPLC hereafter) and parameterized convection (PARAM hereafter) in representing the two extreme precipitation cases around San and Kenieba (Figure 1).

For EXPLC, the parameterization for deep and shallow convection is switched off and, for PARAM, convection is parameterized using the Tiedtke–Bechtold scheme (Bechtold *et al.*, 2008; Tiedtke, 1989). Within the parent domain at 26-km grid spacing, the two nested domains, R3B07 and R3B08, feature successively halved grid spacings of 13 and 6.5 km, respectively (Reinert *et al.*, 2018). The three domains considered for the present study are shown in Figure 1. The initial and boundary conditions for the parent domain are taken from ERA5. The lateral boundary conditions for the two inner domains are updated every six hours. Otherwise, the model configuration matches the operational ICON settings with prescribed sea-surface temperatures and aerosol properties, as is used in Pante and Knippertz (2019).

### 3.2 | Spatial verification methods

The performance of ICON (EXPLC and PARAM) and ERA5 ("test products" hereafter) in representing precipitation is assessed using two spatial verification methods: the fractions skill score (FSS) and the structure–amplitude–location (SAL) score. For both scores, the rainfall fields of all products were aggregated to the same spatial resolution of 0.25° × 0.25° to ensure comparability. Neither the FSS nor SAL is computed for the whole simulation domain of ICON, but rather within a

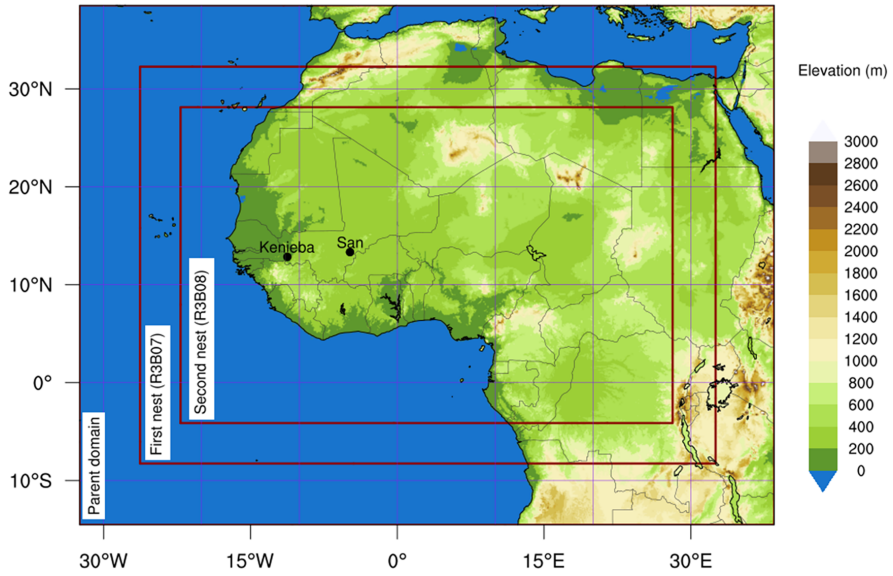


**FIGURE 1** Map showing the terrain elevation (shading) for large parts of Africa, locations of the weather stations of the two Malian cities under study (Kenieba and San, black dots), and the spatial extent of the domains used for the ICON simulations (dark rectangles). The first nest (R3B07 of the ICON nomenclature: Zängl *et al.*, 2015) is the coarser domain with a model resolution of $\Delta x = 13$ km and a model timestep $\Delta t = 120$ s, whereas the second nest (R3B08) is the finer domain with resolution of $\Delta x = 6.5$ km and $\Delta t = 60$ s. [Colour figure can be viewed at wileyonlinelibrary.com]

$6° \times 6°$ box around the individual (subjectively identified) vortex centers in EXPLC, PARAM, and ERA5. This is performed in a Lagrangian way, such that the boxes in each product shift according to the movement of the vortex at each timestep. In this way, the focus is on the evaluation of the spatial distribution of vortex-related rainfall. Through visual inspection, the chosen range of the domain at $6° \times 6°$ encompasses the full extent of the vortex structure identified in ERA5 and the ICON simulations as well as vortex-related rainfall in IMERG in both case studies. Moreover, the effect on the FSS and SAL due to differences in propagation speed of the rainfall systems is minimized. We note that, for IMERG, the center of the box is always set to that in ERA5. For the sake of simplicity, the term "vortex domain" is used for the above-mentioned box in descriptions of FSS and SAL below.

### 3.2.1 | Fractions skill score (FSS)

The FSS method, introduced by Roberts and Lean (2008) and expanded further by Roberts (2008), determines the spatial scale at which the test products become skillful regarding precipitation. It relies on the "neighborhood" approach, that is, a squared domain around a target grid point with iteratively increasing length of $n$ pixels, over which the rainfall field is verified against a reference (here, IMERG).

The first step in computing the FSS is the creation of a binary field for each of the test products and IMERG, where grid points with rainfall values above (below) a threshold are assigned a value of one (zero). In our case, the FSS is used to assess the ability of the models to predict extreme rainfall. Thus, the 95th percentile of all rainfall values (including dry grid points) within the vortex domain was chosen as the threshold, which is determined for each individual product and timestep. A percentile threshold rather than an absolute threshold is applied, such that, ideally, both test products and IMERG end up with the same number of grid points with the value of 1 after filtering. To obtain the threshold, the values of all grid points were sampled and sorted in ascending order, from which the 95th percentile value was determined. Then all values below this threshold value were set to zero, which yields a filtered field of the most intense rainfall for each product and timestep. On average, the 95th percentile corresponds to 53.15 mm in IMERG, 26 mm in EXPLC, 31.85 mm in PARAM, and 25.5 mm in ERA5 at the $0.25° \times 0.25°$ resolution.

The next step is to compare the fractions of grid points in IMERG and the test products that exceed the rainfall threshold within a neighborhood of side length $n$ pixels. The length $n$ is an odd number, with the neighborhood centered around a grid point. This is an iterative process across all grid points in the vortex domain and with successively larger neighborhoods up to a size of $n = 2N - 1$, where $N$ is the number of grid points on the longest side of the vortex domain. The comparison is performed using the mean-square error (MSE) between the fractions, where the mean is taken over all grid points. For a neighborhood with side length of $n$ pixels, the FSS is expressed as (cf. Roberts & Lean, 2008):

$$FSS_{(n)} = 1 - \frac{MSE_{(n)}}{MSE_{(n)\mathrm{ref}}} \tag{1}$$

where a perfect score of $FSS_{(n)} = 1$ is only reached when the fraction field of a test product matches that of IMERG perfectly, that is, $MSE_{(n)} = 0$. Here, $MSE_{(n)\mathrm{ref}}$ can be considered as the largest possible MSE (Roberts & Lean, 2008) based on a low-skill reference forecast described in Murphy and Epstein (1989). By ensuring an equal number of threshold-exceeding grid points in IMERG and the test products, the FSS will converge to 1 towards the maximum neighborhood size. The test products are considered skillful once the FSS reaches a threshold value termed $FSS_{\mathrm{uniform}}$. A skillful spatial scale is given by $FSS > FSS_{\mathrm{uniform}} = 0.5 + f/2$, where $f$ is the observed fractional rainfall coverage over the vortex domain. For a deeper and more detailed discussion of the FSS, we refer the reader to Roberts and Lean (2008). In the present work, the calculation of FSS was performed using the R package "fss" (Pocernich, 2015).

### 3.2.2 | Structure–amplitude–location (SAL) method

The SAL method (Wernli *et al.*, 2008) consists of a three-component, object-based quality measure comparing rainfall objects between IMERG and the test products, where deviations in the structure (S component), amplitude (A component), and location (L component) of precipitation objects are quantified. Again, the 95th percentile value of rainfall at each step is used to delineate the precipitation objects in the vortex domain. In general, all scores contain standardized terms where the S, A, and L components range between $[-2, 2]$ and $[0, 2]$, respectively. Here, a value of zero indicates a perfect result for all scores. The S component evaluates the size distribution of precipitation features. Positive values imply too large precipitation objects in the test products. The A component measures the relative deviation of the domain-averaged precipitation amounts, with positive values indicating an overestimation of the rainfall magnitudes in the test products compared with IMERG. Finally, the L component quantifies two types of location error. A first term L1

measures the displacement of the centers of mass of the precipitation fields between IMERG and the test products. Through normalization with the largest possible distance of two grid points in the vortex domain, L1 ranges between [0, 1]. However, since L1 evaluates the precipitation fields as a whole, a second term L2 provides additional information about errors emerging from the individual rainfall objects and quantifies the average distance between the center of mass of the precipitation field and individual precipitation objects. Like L1, L2 is defined within [0, 1]. Adding L1 and L2 up yields the total L component. We refer the reader to Wernli *et al.* (2008) for a full formulation of all SAL terms.

### 3.3 | Spectral filtering of tropical waves

To provide insight into the potential role of tropical waves on the two extreme events, the spectral (wavenumber–frequency) wave filtering approach by Wheeler and Kiladis (1999) was applied to six-hourly, normalized rainfall anomalies from IMERG around the periods of interest. The spectral analysis was performed for the latitudinal band 5°–15°N and thus centered around the latitudinal position of San and Kenieba. Here, the wave types considered are the Madden–Julian Oscillation (MJO), equatorial Rossby waves (ER), mixed Rossby–gravity waves (MRG), Kelvin waves, and tropical disturbances (including AEWs), the filter settings of which are the same as in Schlueter *et al.* (2019b). Following the concepts of, for example, Riley *et al.* (2011), Yasunaga and Mapes (2012), and Schlueter *et al.* (2019a), an evaluation of the temporal evolution of the local wave phases and magnitudes during both cases is undertaken by determining the wave-filtered rainfall anomalies and their time derivatives, both of which are standardized by the respective standard deviation value. Within this phase–magnitude spectrum, eight (cyclic) wave phases P1–P8 according to Schlueter *et al.* (2019a) are defined, where P4–P6 indicates the convectively favorable and P8–P2 the convection-suppressing range. The magnitude of the wave signal is defined by the squared sum of standardized rainfall anomaly and time derivative, represented visually by the distance to the origin. As in Nicholson *et al.* (2022), for each of the eight wave phases, the 95th and 99th percentiles are indicated to assess the extremeness of the wave amplitude.

## 4 | OBSERVED RAINFALL AND ASSOCIATED WEATHER SYSTEMS

### 4.1 | Observed station rainfall

In the following sections, both the San and Kenieba cases are analyzed with respect to the spatio-temporal structures of rainfall in observations. To illustrate the rainfall magnitude of the events, the evolution of daily gauge precipitation at the stations of San in August 2012 (Figure 2a) and Kenieba in August 2019 (Figure 2b) is shown (shading). The San case is clearly visible as a distinct spike on August 8 in the rain-gauge data with magnitude 127 mm, exceeding all other daily rainfall amounts in August 2012 (Figure 2a). Similarly, the 126-mm peak of the Kenieba case is clear on August 25, 2019 (Figure 2b). Both cases are extreme, in that these rainfall amounts exceed the 99th percentile values (i.e., 80 mm for San and 100 mm for Kenieba) of all recorded wet days within the respective 20-year sample (2000–2019) of the stations. Furthermore, both cases were embedded within marked wet spells, indicated by multiple preceding and succeeding rainfall

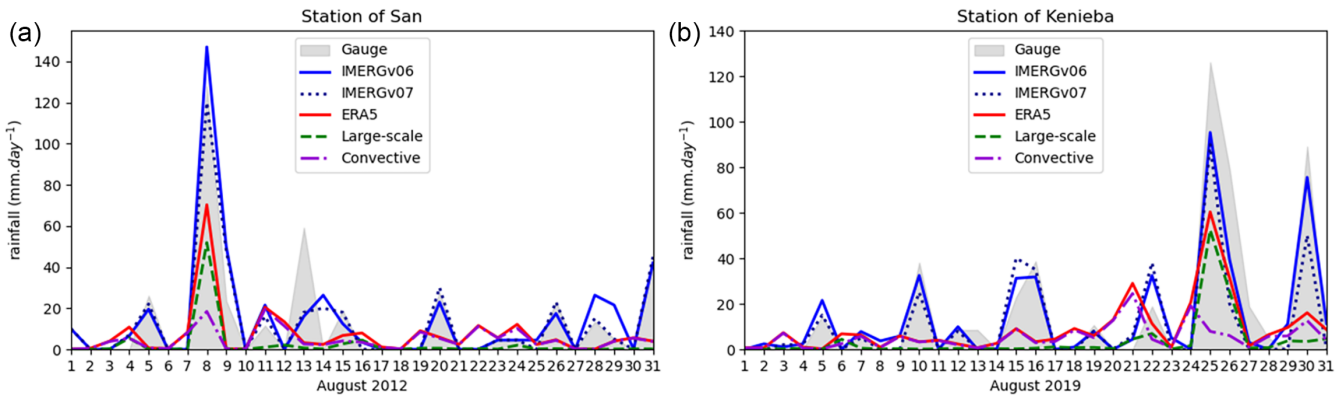


**FIGURE 2** Evolution of daily rainfall at (a) the station of San in August 2012 and (b) the station of Kenieba in August 2019, from rain-gauge data (shaded), IMERG estimates (V6B and V7), and total ERA5 rainfall and its partitions "grid-scale" and "convective" rainfall. [Colour figure can be viewed at wileyonlinelibrary.com]

events. Within seven days, from August 8–14, 2012, the station of San recorded 225 mm of rainfall. Also, the period around the Kenieba case was particularly wet, with an additional rainfall of 191.8 mm between August 26 and 30, 2019. Thus, approximately 318 mm of rain were accumulated at the station of Kenieba within a span of seven days.

For comparison, IMERG (V6B and V7) and total ERA5 rainfall estimates are included in Figure 2. They are calculated as the $0.5° \times 0.5°$ mean values at the four closest grid points to each of the stations of San and Kenieba. The ERA5 estimates are partitioned further into the "grid-scale" and "convective" rainfall, which constitute total ERA5 rainfall when combined. For the San case (Figure 2a), IMERG is able to capture the extreme event, although daily rainfall is overestimated by roughly 20 mm by V6B. A brief comparison between IMERG V6B and V7 shows that V6B tends to peak higher than V7 for extreme daily rainfall. While not necessarily a sign of better quality, V6B matches observed intense rainfall overall more closely than V7 according to auxiliary tests, as mentioned in Section 2. In the rest of the article, we will refer to V6B only. Conversely to IMERG, but not surprisingly, ERA5 strongly underestimates the event, which is partly rooted in the poor handling of rainfall by the convection parameterization scheme in IFS, and ultimately in limitations imposed by the coarse spatial resolution at 0.25° (Jiang *et al.*, 2021; Lavers *et al.*, 2022; Rivoire *et al.*, 2021). However, relative to their own 20-year samples of daily rainfall, both IMERG and ERA5 values for this event exceed the 99th percentile (not shown). In other words, the San case was extreme within the climatologies of the respective datasets. In addition, the San case is mostly of "large-scale" nature in ERA5, indicating that the area of convective activity was sufficiently large to be resolved by IFS. For the Kenieba case (Figure 2b), both IMERG and ERA5 underestimate the event on August 25, 2019 slightly, but still reach the 99th percentile of August rainfall in their climatologies. Similarly to the San case, the majority of the total ERA5 rainfall in the Kenieba case is constituted by the "large-scale" scheme. Being an observational dataset, IMERG performed well overall in estimating the magnitude and timing of rainy days.

## 4.2 | Spatio-temporal evolution of extreme rainfall

### 4.2.1 | San case

Figure 3 highlights the spatio-temporal evolution of three-hourly IMERG rainfall during the San case at selected timesteps between and August 6 and 8, 2012. On August 6 at 0600 UTC, that is, two days prior to the main event, multiple weakly organized rainfall structures are present over southern Niger around $5° - 10°$E (system A in Figure 3a), the leading few of which clustered and evolved into a squall line 12 hours later (Figure 3b), gradually approaching San. Figure 3c depicts two organized rainfall systems. The first reached the station of San around 0600 UTC on August 7, 2012. Several convective cores had developed in the wake of this squall line, which seemed to reinforce the second rainfall core (system B in Figure 3c) arriving at San in the afternoon (Figure 3d). This second rainfall core impacted San and surrounding areas for about 12 hours (see system B in Figure 3c,d). Ultimately, by early evening of August 8, this convective cluster has left the San region (Figure 3f). Overall, the passage of multiple intense convective systems contributed to the extreme nature of the San case. In addition, the event was widespread and reached other synoptic stations in southern Mali, causing 56.9 mm in Segou, 61.8 mm in Bamako-Senou, 90 mm in Koutiala, and 48.5 mm in Sikasso (not shown). With rainfall already occurring the days before (see Figure 2a), this situation led to severe damage to crops and cattle and destroyed many houses (OCHA, 2012).

### 4.2.2 | Kenieba case

Figure 4 depicts the evolution of three-hourly IMERG rainfall during the Kenieba case around August 25, 2019. Two days prior to the event on the morning of August 23, 2019, an organized rainfall system was active around the locality of Hombori (system A in Figure 4a). This cluster moved westward and rapidly developed several highly active convective cores (Figure 4b), which organized into a curved, zonally oriented band of strong rainfall south of Mali, as well as an intense, circular shaped system just east of Kenieba (systems B and A, respectively, in Figure 4c). Overall, the bow-like spatial pattern of strong convection hints at the existence of a rotational flow, that is, a vortex, in the low- to mid-tropospheric horizontal flow field along which the rainfall systems intensify. Having arrived on the morning of August 24, 2019, the convective cluster subsequently influenced Kenieba for more than 24 hours, as it began to decelerate and eventually stall over the course of August 24 and 25 (Figure 4d–f). The meteorological aerodrome (METAR) report at Kenieba airport indicated that the 126 mm raainfall on August 25, 2019 were accumulated between August 24 at 1200 UTC and August 25 at 1800 UTC. Most of the synoptic stations in the country were affected by this event. 61 mm were recorded at the station of San, 51 mm in Segou, 28 mm in Bamako, 88.5 mm in Koutiala, 79.3 mm in Sikasso, 73.6 mm in Nara,

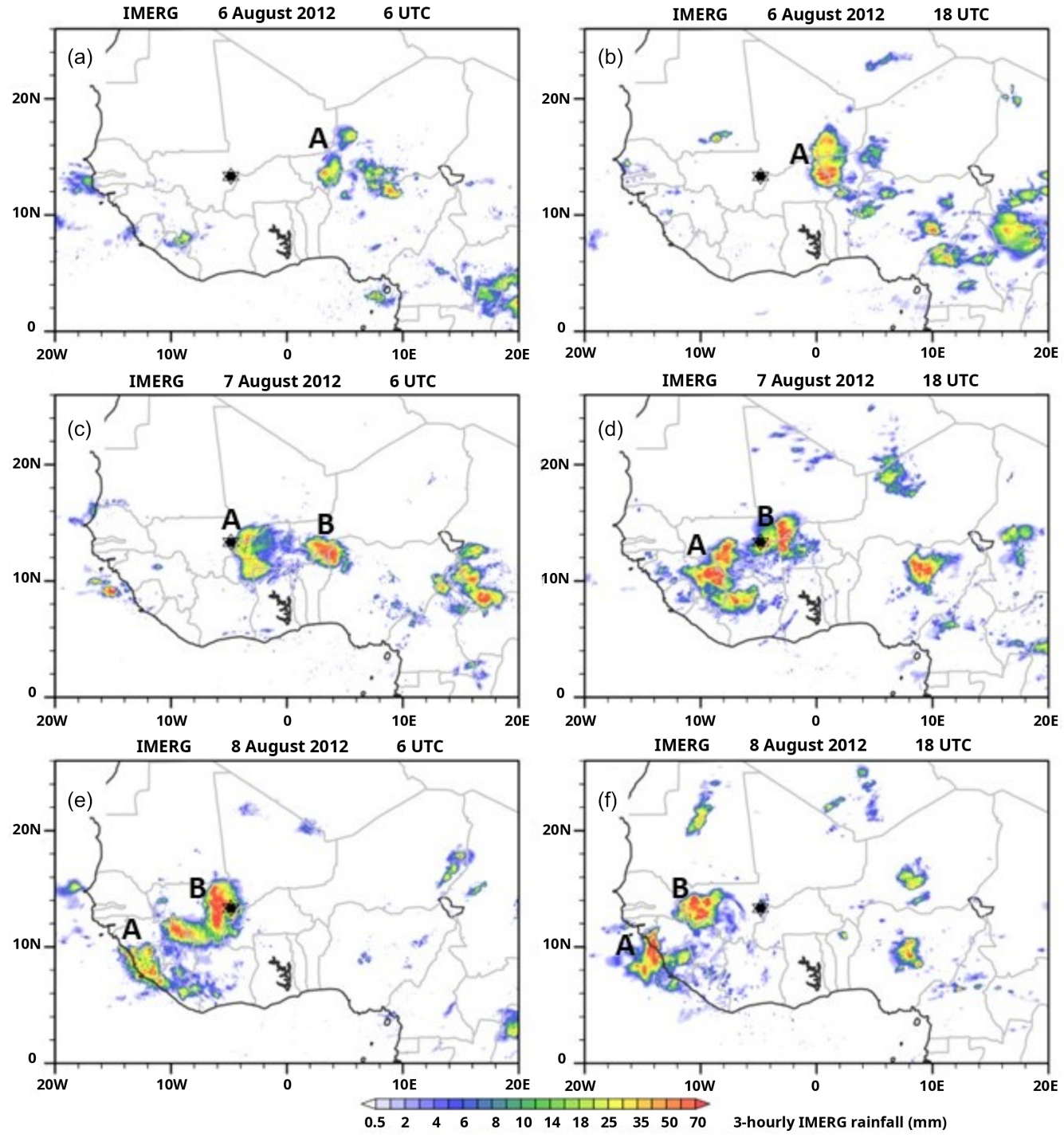


**FIGURE 3** Evolution of three-hourly IMERG rainfall at important timesteps between August 6 and 8, 2012. The star marker shows the location of San. The indicated time of day (in UTC) denotes the end of the accumulation period, for example, 0300–0600 UTC is indicated as 0600 UTC. Two major westward-propagating rainfall systems are identified and labeled as A and B. [Colour figure can be viewed at wileyonlinelibrary.com]

and 76.9 mm in Kayes (all not shown). Aside from this, and in contrast to the San case, where the convective activity is largely confined to the Sahel in the north, the period around the Kenieba case was also marked by enhanced rainfall activity deep in the Sahara, extending to latitudes beyond 20°N, which, as seen later, was facilitated by a remarkable and widespread northward extension of air-masses with high low-tropospheric moisture.

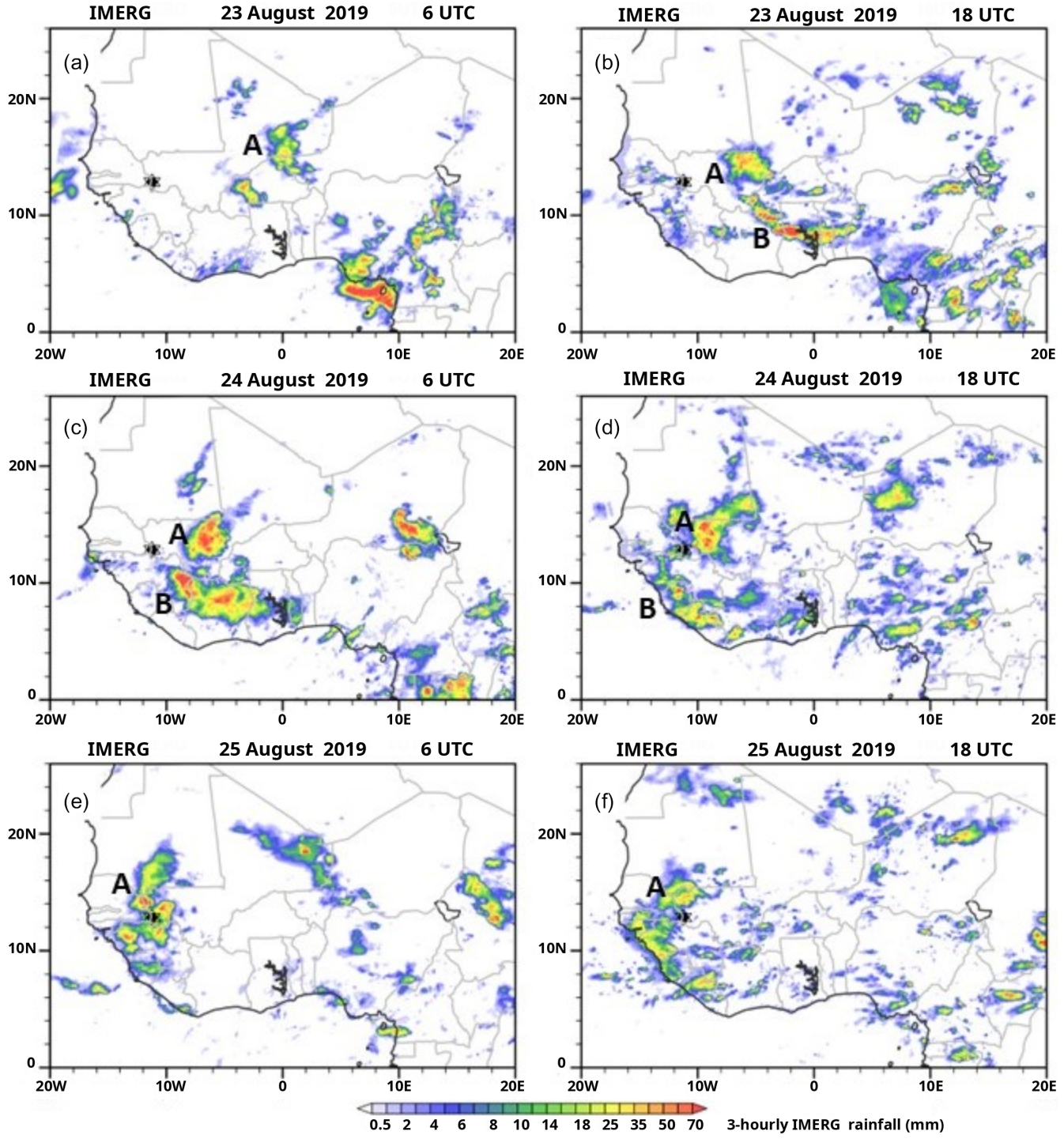


FIGURE 4 As Figure 3 but for the Kenieba case, showing selected timesteps between August 22 and 25, 2019. [Colour figure can be viewed at wileyonlinelibrary.com]

## 4.3 | Evolution of associated weather systems

This section evaluates the dynamics and synoptic evolution of weather systems at selected timesteps prior to and during the two events.

### 4.3.1 | San case

Figure 5 depicts the spatio-temporal evolution of the strongest moisture convergence (green contours), the mass-weighted mean of horizontal wind between 925 and 600 hPa (arrows), and the relative location of the heat

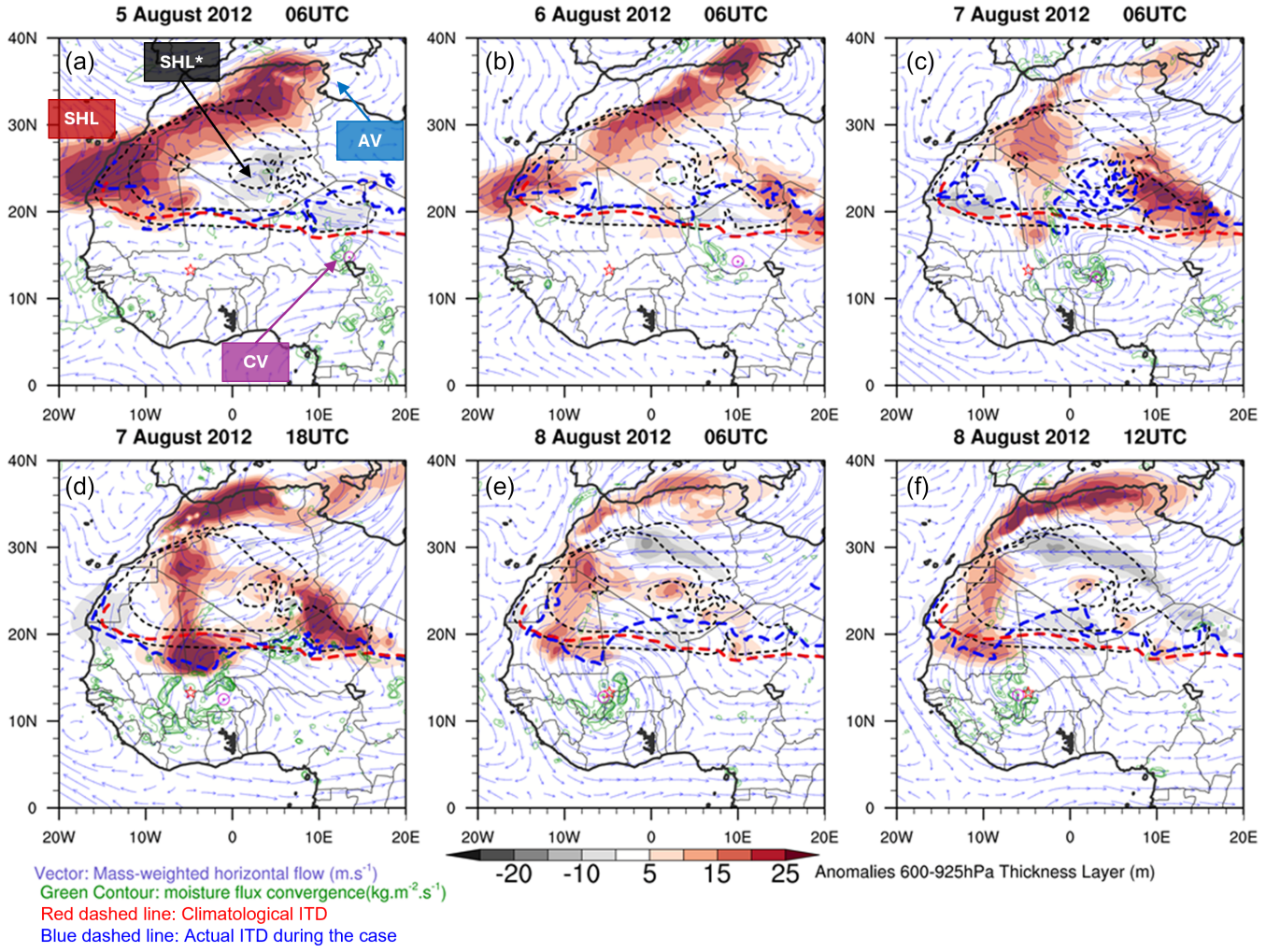


**FIGURE 5** Evolution of weather systems at selected timesteps prior to and during the San case from August 5–8, 2012 over West Africa. The star marker and the circled dot show the positions of San and the center of the rain-bearing cyclonic vortex, respectively. Vectors denote 925–600 hPa mass-weighted flow, shadings indicate anomalies of the 925–600 hPa layer thickness (used as proxy for the location of the heat low) with respect to the 1981–2010 long-term monthly mean (thin dashed contours), the thick dashed lines indicate the actual and climatological ITD positions, defined by the 14°C isodrosotherm at 2 m, and moisture flux convergence with contour levels at $-12 \times 10^{-3}$ to $-0.5 \times 10^{-3}$ kg · m$^{-2}$ · s$^{-1}$. In (a), SHL, SHL*, AV, and CV denote the Saharan heat low, the climatological SHL in the month of August, the anticyclonic vortex over the Mediterranean and Northern Africa, and the cyclonic vortex, respectively. [Colour figure can be viewed at wileyonlinelibrary.com]

low defined as layer thickness, as well as the intertropical discontinuity (ITD) prior to and during the San case. The SHL location is determined using the low-level thickness layer between 925 and 700 hPa as in Lavaysse *et al.* (2009). The anomalies (shadings) from the long-term August mean of the low-level layer thickness (i.e., climatological SHL position; center labeled as SHL*) depict the change in the location of the SHL, where anomalously high positive values indicate its position.

A few days prior to the San case, the SHL is located anomalously to the west at the Atlantic coast (Figure 5a,b). At its climatological position over southeastern Algeria (5°E, 25°N; labeled SHL*), the layer thickness is lower than normal, which appears to be due to ventilation from an anticyclone over the Mediterranean Sea (labeled AV). At the same time, the mass-weighted flow indicates the existence of a weak cyclonic circulation over Lake Chad (15°E, 15°N; labeled CV), from where it starts moving westward. By August 7 (Figure 5c), one day prior to the San case, this vortex has intensified visibly over western Niger (4°E, 12°N), where it exhibits pronounced moisture convergence in its center. Furthermore, together with a strengthened anticyclone over the Mediterranean Sea, a continuous northeasterly flow extending from the Mediterranean Sea to the western flank of the cyclonic vortex is established. Over the course of August 7, this

leads to a southward bulge of the ITD to the northwest of the cyclonic vortex, which is likely due to a southward advection of dry airmasses related to the SHL. The consequence is a local maximum of layer thickness anomaly just north of San (5°W, 18°N; Figure 5d). This is the time when the station (star marker) was passed by multiple intensified convective cores in the wake of the squall line (cf. Figure 3d). The southward intrusion of dry air and the subsequent lifting of moist airmasses probably facilitated the intensification of these convective cores, similar to the effect of drylines known in the midlatitudes (e.g., Johnson & Hitchens, 2018). In this regard, Klein and Taylor (2020) outlined a mechanism where the convergence of moist monsoon airmasses and a southward excursion of drylines and the ITD, the latter leading to dry anomalies in soil moisture and stronger heat fluxes, creates enhanced convective instability, which facilitates the intensification or even the generation of MCSs. Indeed, pronounced soil moisture gradients prevail during the San case along the storm path (not shown), which overall might have promoted the initiation and maintenance of these successive convective cores. In any case, the cyclonic vortex intensifies further and likely causes the convective systems to strengthen as well (cf. Figure 3e,f) while providing further moisture, as seen by pronounced moisture convergence in the vortex center during the San case (Figure 5e,f).

### 4.3.2 | Kenieba case

Similarly to the San case, the Kenieba case occurred during a period with a weakening of the SHL, but to a considerably stronger extent. Figure 6 shows the environmental conditions up to three days prior to the event on August 25, 2019. On August 22, the SHL is located at the

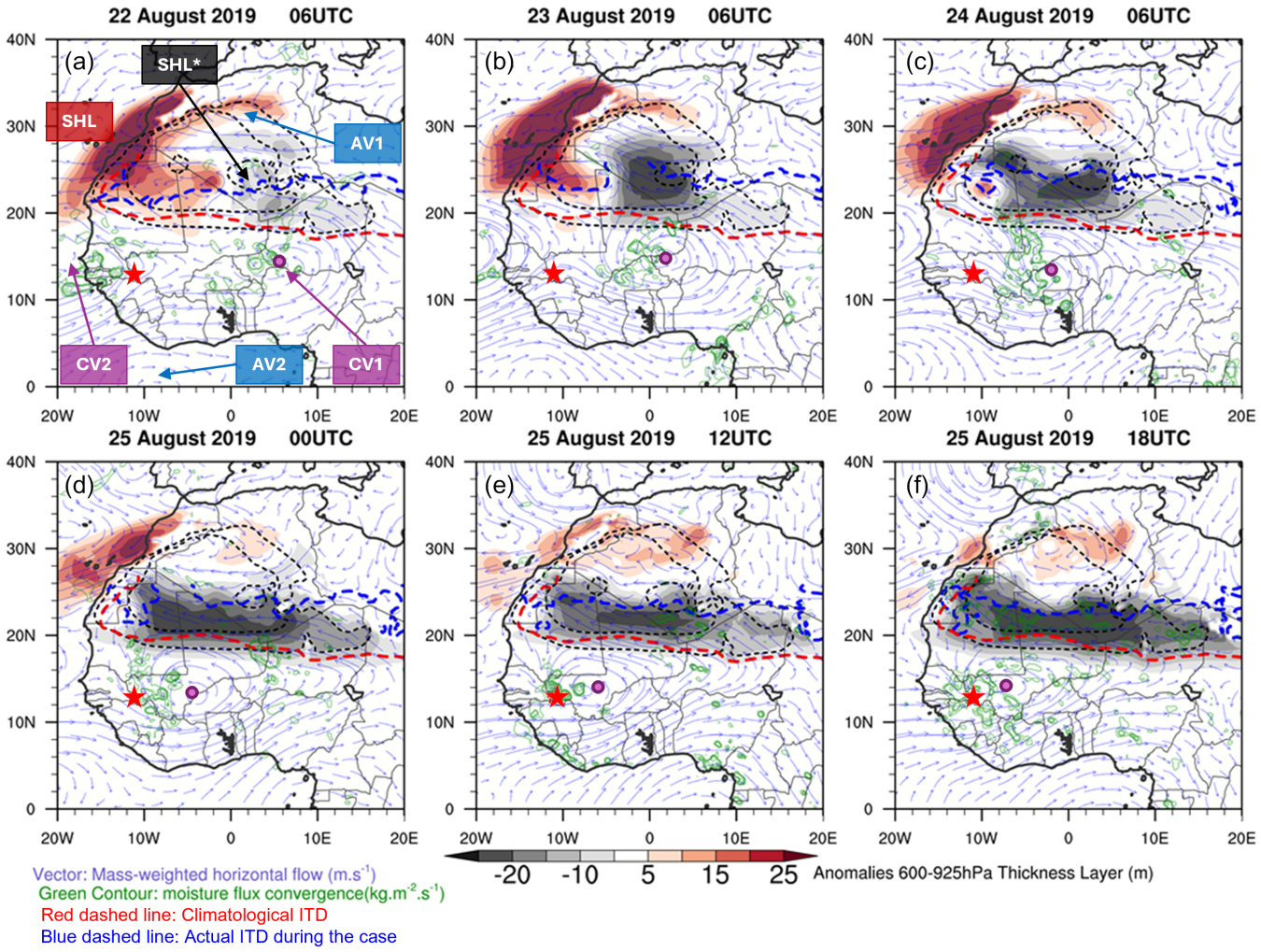


**FIGURE 6** Similar to Figure 5, but around the Kenieba case from August 22–25, 2019. In (a), AV1 and CV1 refer to the relevant anticyclonic and cyclonic vortices, respectively, over the continent, while AV2 and CV2 refer to the vortex couple over the eastern Atlantic. [Colour figure can be viewed at wileyonlinelibrary.com]

coast of northwestern Africa after being pushed westward by a weak negative anomaly in the 600–925 hPa thickness layer over southern Algeria (Figure 6a). The latter is sustained by a cyclonic vortex (labeled CV1) over southern Niger (circle marker, 6°E, 13°N) and a weak anticyclone (labeled AV1) over northern Algeria (7°E, 33°N), both advecting cooler and moister air into the Sahara. At this point, a pronounced northward shift of the ITD to 25°N (blue dashed line), far from its climatological position at 20°N (red dashed line), is evident in almost the entire domain, which emphasizes a deep moistening of the southern Sahara, stronger than during the San case. This is likely facilitated by a north–south aligned vortex couple over the Atlantic (labeled AV2 and CV2), which establishes a low-level, anomalous westerly "conveyor belt" of moist and cool air over the Guinea Coast region. Eventually, these airmasses are picked up by the cyclonic vortex over Niger and transported northward into the Sahara on its eastern flank. Over the days preceding the Kenieba case, the negative layer thickness anomaly intensifies and extends westward due to the strengthening of the cyclonic and anticyclonic vortices over land (Figure 6b) and their gradual westward displacement (Figure 6c–f), which leads to an erosion of the SHL. By the time of the event (Figure 6d–f), the entire Guinea Coast region is under the influence of a southwesterly flow, driven by the cyclonic vortex now located east of Kenieba at 5°W, 13°N. Thus, Kenieba (star marker) is located at its western flank and in an area of enhanced moisture flux convergence (green contours), which likely played a key role in the development of extreme rainfall over the station. Furthermore, it is suggested that the pronounced moistening of the southern Sahara prevented strong evaporation to an extent that allowed the vortex to wrap sufficient moisture to its downstream flank for the build-up of enhanced precipitation.

## 4.4 | Role of equatorial wave activity

Regarding an understanding of the dynamical evolution of extreme Sahelian rainfall, highly organized convective systems such as those shown in this article, as well as in other studies (e.g., Engel *et al.*, 2017), are often associated with the presence of AEWs, but have also been identified to link with other equatorial waves (e.g., Lafore *et al.*, 2017). Following the application of the spectral wavenumber–frequency filtering approach described in Section 3.3, an overview of equatorial wave activity around both the San and Kenieba cases is given in Figure 7, where the Hovmöller diagram displays the propagation of convectively favorable (i.e., positive) wave phases (envelopes) during the periods of interest. The respective time and date of the events at the locations of the San and Kenieba stations are indicated by the intersection of the horizontal and vertical lines in this longitude–time space.

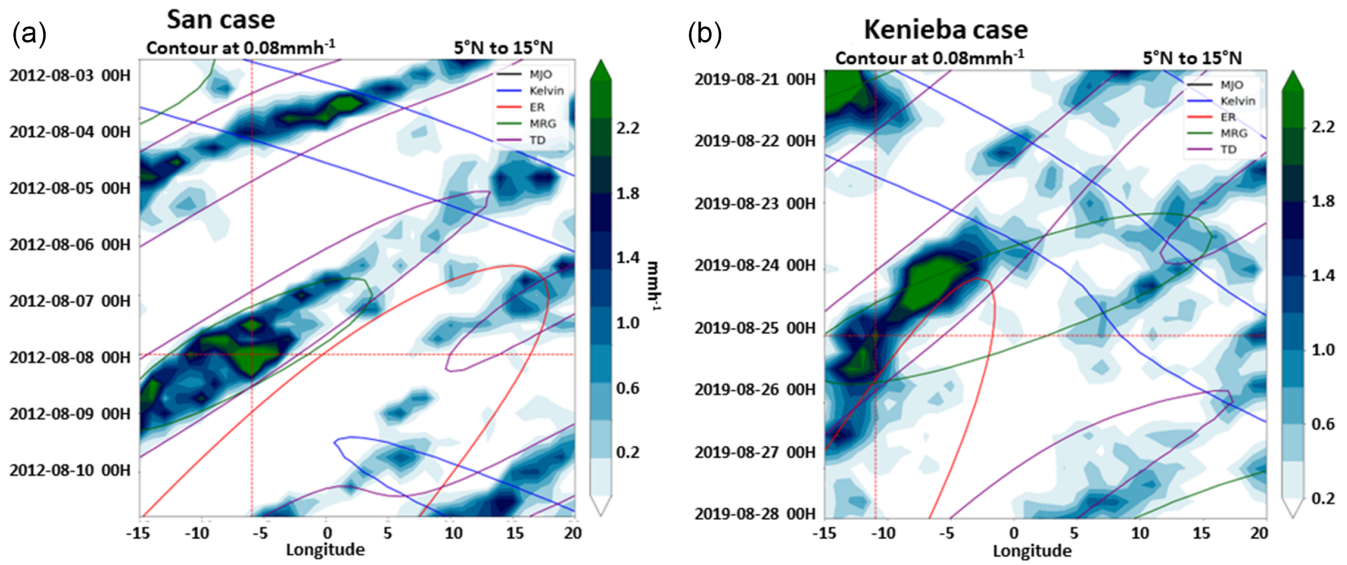


**FIGURE 7** Hovmöller diagram of wave-filtered six-hourly IMERG rainfall within the 5°–15°N latitude band for the periods (a) August 3–10, 2012 around the San case and (b) August 21–27, 2019 around the Kenieba case. Vertical and horizontal lines indicate the position of the stations and the event time, respectively. Contours denote a wave-filtered rainfall rate above 0.08 mm · $h^{-1}$, based on the wave types indicated in the legend. The shadings indicate the meridionally averaged six-hourly IMERG rainfall. The diagram was created using the wavenumber frequency filtering concept of Wheeler and Kiladis (1999) and parameters in Schlueter *et al.* (2019b). [Colour figure can be viewed at wileyonlinelibrary.com]

The previously analyzed low-tropospheric vortices are clearly identified as westward-propagating tropical disturbances in both cases (TDs, purple contours in Figure 7a,b), which move alongside the rainfall signals causing the extreme events (shaded features). Each of the TD passages during the events was preceded by another positive TD phase by roughly four days. This falls well within the periodicity of AEWs (e.g., Burpee, 1972; Fink & Reiner, 2003), which supports presumptions that both extreme rainfall cases and the emergence of low-level vortices therein were driven by AEWs. Furthermore, a common feature in both cases is an embedded, westward-moving positive MRG phase, which appears to coincide with an intensification of convective activity. The concept of AEW–MRG interactions and mutual amplification abilities over Africa is not unknown and has been the subject of extended evaluation in Yang *et al.* (2018) and Cheng *et al.* (2019). However, it should be noted that, since the ranges of frequency and wavenumber for the filtering of TD and MRG partially overlap (see Schlueter *et al.*, 2019b), signals of both waves are not entirely distinguishable. Therefore, it is possible that TDs project onto MRGs and vice versa, which might be the case for the San event (Figure 7a). Regarding other wave types, the development of the TD and MRG in the Kenieba case (Figure 7b) could have benefited from the existence of an eastward-propagating Kelvin wave, which intersects the waves already further upstream around and east of the zero meridian, respectively. Although also existent in the San case (Figures 7a), a potential influence of the Kelvin wave on the two waves prior to the event is less obvious, but might have facilitated the intensification of the TD. Overall, it appears that both cases were largely influenced by the fast equatorial wave modes. Out of the slower waves, only ER signals are identified, which might have had an influence at least during the Kenieba case (Figure 7b). Overall, the analysis is consistent with the statistical results discussed in Peyrillé *et al.* (2023), which document the prevalent role of AEWs for extreme precipitation events in the region, with the Kelvin wave enhancing the convection and the ER being a potential large-scale driver.

To complement the Hovmöller analysis, Figure 8 illustrates the phase–amplitude characteristics of the most relevant wave, that is, TD, during the San (Figure 8a) and Kenieba (Figure 8b) cases from an Eulerian perspective. As underlined by Rasheeda Satheesh *et al.* (2025), who demonstrated that combined information on wave phase and amplitude can improve forecasting skill of

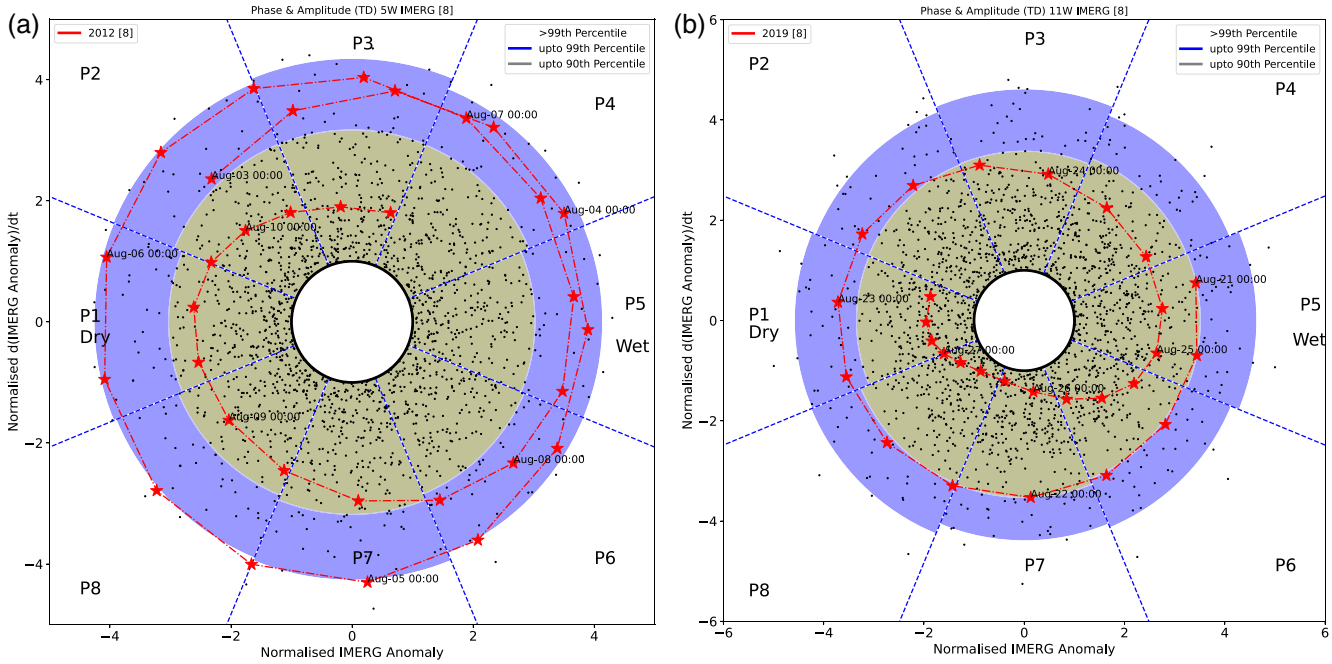


**FIGURE 8** Phase diagram of the local (i.e., based on the station longitude) TD wave activity during both case studies, defined by the standardized IMERG rainfall anomaly (*x*-axis) and its time derivative (*y*-axis). The spectrum is subdivided into eight phases, where P1 and P5 denote the peak dry and wet phases, respectively. The star markers indicate each timestep during the respective cases, which form the dashed trajectory in the phase spectrum. Timesteps with a standardized value < 1, that is, being within the white center circle, denote an inactive wave. For each of the eight wave phases, the inner and outer shaded areas encompass the sample (scatters) of local wave amplitudes up to the 90th and 99th percentiles, respectively. Scatters outside the boundary of the outer shaded area indicate the strongest 1% amplitudes. Note the different axis range, that is, range of wave magnitudes. (a) San TD, (b) Kenieba TD. [Colour figure can be viewed at wileyonlinelibrary.com]

rainfall, this diagnostic provides additional quantitative insight into the magnitude and phase of wave activity in the context of extreme precipitation during both events. The local wave phase P1–P8, at the longitude of the San and Kenieba stations, respectively, can be inferred by the dashed, star-marked trajectory within the phase room, where the local wave amplitude is further indicated by the radial distance from the plot center. Moreover, the shaded areas in each wave phase encompass the sample of local wave amplitudes for the period 2001–2019 (August data only), where the upper boundaries of the inner and outer areas delineate the 90th and 99th percentiles, respectively. If the trajectory is located inside the center circle, that is, having a standardized amplitude of less than 1, the wave is considered to be inactive; otherwise it is active.

Based on the extent of the shaded areas, TDs typically attain higher standardized amplitudes than other tropical wave types (e.g., MRGs, not shown), which reflects how frequently intense rainfall in Sahelian MCSs is coupled with the existence of TDs. During the San case, two full TD/AEW cycles influence the region, with the second corresponding to the main event on August 7–8. Both occur within the convectively favorable phases P4–P6 and display exceptionally strong amplitudes—within the upper 10% and at times even approaching the 99th percentile of the climatological sample. This unusually intense TD signal coincides with the peak of convective activity and, eventually, the observed daily rainfall maximum of 127 mm. In contrast, the Kenieba case is characterized by a weaker and slower TD signal (about 1.5 cycles over the analysis period), yet it produced a comparable rainfall total (126 mm). This indicates that, while amplitude and phase of the TD govern the regional-scale convective environment, the final rainfall amount depends on mesoscale factors such as system longevity and organization.

# 5 | EVALUATION OF ICON SIMULATIONS

## 5.1 | Comparison of rainfall fields

Both the San and Kenieba cases were simulated with ICON, which was initialized several days prior to each verification date in order to accommodate important dynamical features discussed in the previous section. As detailed in Section 3, two experiments for each case are conducted: ICON with convective parameterization enabled (PARAM) and disabled (EXPLC). To facilitate the comparison, three-hourly rainfall in IMERG and the ICON experiments is displayed in Hovmöller diagrams for the San (Figure 9, left column) and Kenieba (Figure 9, right column) cases. Here, rainfall was meridionally averaged within a 5° band with the center latitude at the coordinates of San and Kenieba, respectively.

### 5.1.1 | San case

During the period of the San case (horizontal shading), the longitude of the station (vertical dashed line) experiences the passage of two major rainfall streaks in IMERG (Figure 9a), which reflects both the squall line and the intense convective cells in its wake (see Figure 3). EXPLC is able to capture the entire westward propagation of the convective cells, although at considerably lower intensity and with a delay in arrival of roughly 12 hours with respect to the first streak (Figure 9b). Furthermore, a more detailed inspection of the precipitation fields reveals that the spatial extent of the rainfall systems in EXPLC is underestimated compared with IMERG (not shown), which partly explains the weaker signals. Nonetheless, signs of consecutive passages of convective systems are represented in EXPLC. Their propagation speed is also comparable with the estimation in IMERG ($9\ m \cdot s^{-1}$). The convective activity prior to the San case is generally overestimated but somewhat misses the intensity of the rainfall event around August 4, 2012. The simulation with PARAM likewise captures the westward propagation of rainfall systems (Figure 9c), which suggests that the evolution of the San case was steered by large-scale dynamics. The San region experiences the passage of a single but more intense rainfall streak in PARAM with lower translation velocity ($7\ m \cdot s^{-1}$) compared with EXPLC ($8\ m \cdot s^{-1}$), the structure of which shows less "noise".

### 5.1.2 | Kenieba case

The Kenieba case is marked by westward-propagating systems that become organized and intense on August 24, 2019 (Figure 9d). Eventually, this manifests in intense signals at the longitude of Kenieba, lasting for the entire August 25, 2019. Although convective activity associated with the Kenieba case, along with its westward propagation, is visible in EXPLC, the rainfall signals never reached the magnitudes of IMERG (Figure 9e). This is because the rainfall systems in EXPLC failed to organize into convective clusters (not shown), in stark contrast to developments seen in IMERG in Figure 3c. The rainfall signals in the Hovmöller diagram appear very scattered and seem to influence the Kenieba region beyond the period of the Kenieba case. PARAM, on the other hand, shows strong similarities to the convective development in

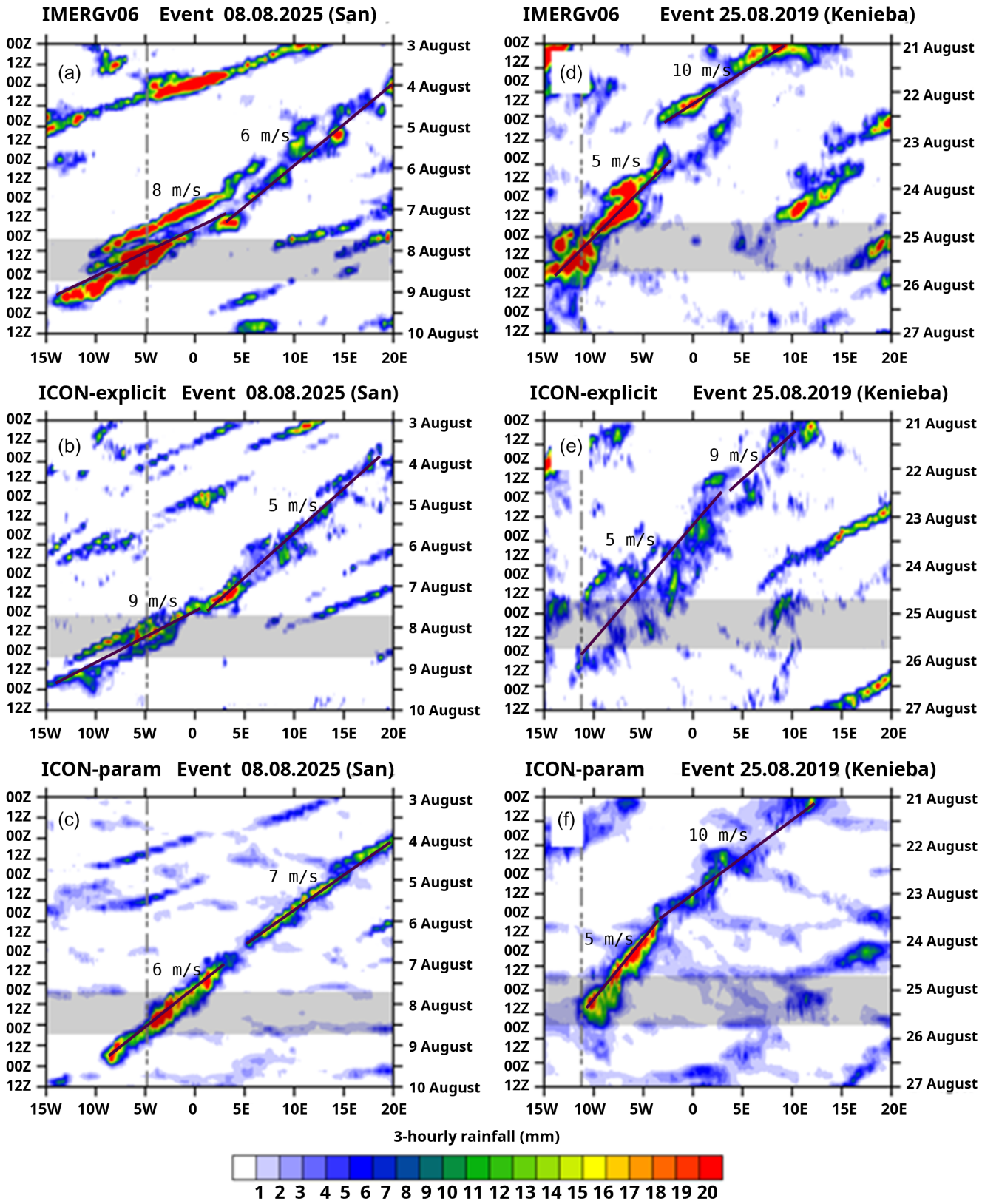


**FIGURE 9** Hovmöller diagrams showing three-hourly accumulated rainfall from (a,d) IMERG, (b,e) EXPLC, and (c,f) PARAM. The panels on the left side depict the extended period prior to and during the San case (August 8, 2012) and panels on the right side prior to and during the Kenieba case (August 25, 2019). Rainfall is averaged over a 5° latitude band centered over the coordinates of San and Kenieba, respectively. The vertical lines indicate the longitudinal positions of San and Kenieba. The horizontal, shaded band refers to the time when the rains were active at San and Kenieba, respectively, according to IMERG. The lines within the rainfall streak related to the investigated MCSs denote estimated velocity slopes with their respective values. [Colour figure can be viewed at wileyonlinelibrary.com]

IMERG (Figure 9f). The rainfall intensification becomes apparent around the same time. However, the subsequent westward propagation in PARAM occurs at a slightly lower pace (at a velocity of 9 $m \cdot s^{-1}$). Moreover, PARAM seems to lack the capability to sustain convection beyond 10°W, which, interestingly, is also apparent in the San case. While a deeper analysis is beyond the scope of this study, it can be speculated whether the influence of the topography of the Guinea Highlands plays a role in the loss of convective organization in PARAM.

Overall, the San and Kenieba cases show rather contrasting outcomes with respect to the performance of explicit convection. In particular, the Kenieba case demonstrates that EXPLC does not necessarily lead to superior results compared with PARAM with respect to the organization of large convective activity. However, EXPLC generally appears more capable of reproducing smaller-scale convective systems and simulating their westward propagation.

## 5.2 | Spatial verification of ICON precipitation fields

This section focuses on the comparison of spatial features of the three-hourly rainfall fields in the ICON simulations with IMERG estimates during both the San and Kenieba events using FSS and SAL (see Section 3) as complementary diagnostics, offering a combined perspective on the spatial scales of model skill and the underlying structural and positional characteristics of simulated extreme rainfall. In the following, they are applied to the timesteps shown in Figures 3 and 4, that is, on three-hourly rainfall. The rainfall fields of ERA5 are additionally evaluated in this analysis to provide the perspective of another product with parameterized convection.

### 5.2.1 | San case

For the San case, Figure 10a depicts the FSS for EXPLC, PARAM, and ERA5 at the selected timesteps from Figure 3, namely at all 0600 and 1800 UTC timesteps from August 6–8, 2012, expressed by the respective median (thick lines) and the extent of the minimum–maximum "ensemble" spread (shaded areas). The FSS level beyond which the product can be considered skillful ($FSS_{\text{uniform}} \sim 0.53$) is marked by the horizontal dashed line. It is evident that the median FSS curves of EXPLC cross $FSS_{\text{uniform}}$ at a smaller spatial scale than ERA5 and PARAM (crossing points at 2.25° versus 3.25° and 4°, respectively). Up until ~ 2.75°, EXPLC also shows a faster increase in FSS, as the neighborhood size increases compared with ERA5 and PARAM. These results indicate that the spatial error regarding the most intense vortex-related rainfall is smallest in EXPLC among all products. The slower increase of the median FSS curves for ERA5 and PARAM at scales below 2° suggests general shortcomings in the spatial placement of the heaviest vortex-related rainfall with parameterized convection. For PARAM, this is generally true across all timesteps considered. Eventually, the curves converge around 4.5°, beyond which little to no distinction can be made regarding the performance of the products. Furthermore, lowering the threshold to the 75th percentile does not close the performance gap between PARAM and EXPLC (not shown).

The performance of the products is evaluated further with SAL in Figure 10b, where the S and A components are plotted on the abscissa and ordinate, respectively. The median values of both are denoted by the dashed lines, as well as in Table 1 for all components. Eventually, the shaded areas show the degree of dispersion of the data points, defined by the minimum and maximum values of the S and A components. The L component of each timestep is depicted by the size of the data points. Recall that a value of zero indicates a perfect result for all components. In general, while the medians show a similar tendency for all products, distinctions between explicit and parameterized convection are notable. EXPLC tends to underestimate the sizes of the rainfall structures compared with IMERG (i.e., negative S values), which is in line with presumptions made in Section 5.1.1 that EXPLC generally struggles with convective organization. This does not seem to be prevalent with parameterized convection. Considering the A component, EXPLC underestimates the rainfall amounts around the vortex, confirming the observations made in the previous section. However, the A-component variability in EXPLC is visibly smaller than for both PARAM and ERA5, partly since the latter show instances of strong overestimation of rainfall. Overall, while rainfall in EXPLC is generally too weak and small, both PARAM and ERA5 appear to have a higher ability to form organized rainfall. The L component is not trivial to interpret, as it consists of two parts (see Section 3). However, both PARAM and ERA5 are more prone to larger location errors (i.e., values around 0.5) than EXPLC, which is reflected in slightly higher median values (Table 1). For ERA5, this is particularly interesting, in so far as it shares the same center location of the 6° × 6° domain as IMERG (see Section 3.2). Therefore, the location errors with parameterized convection are likely the major source of lower skill according to the FSS as well.

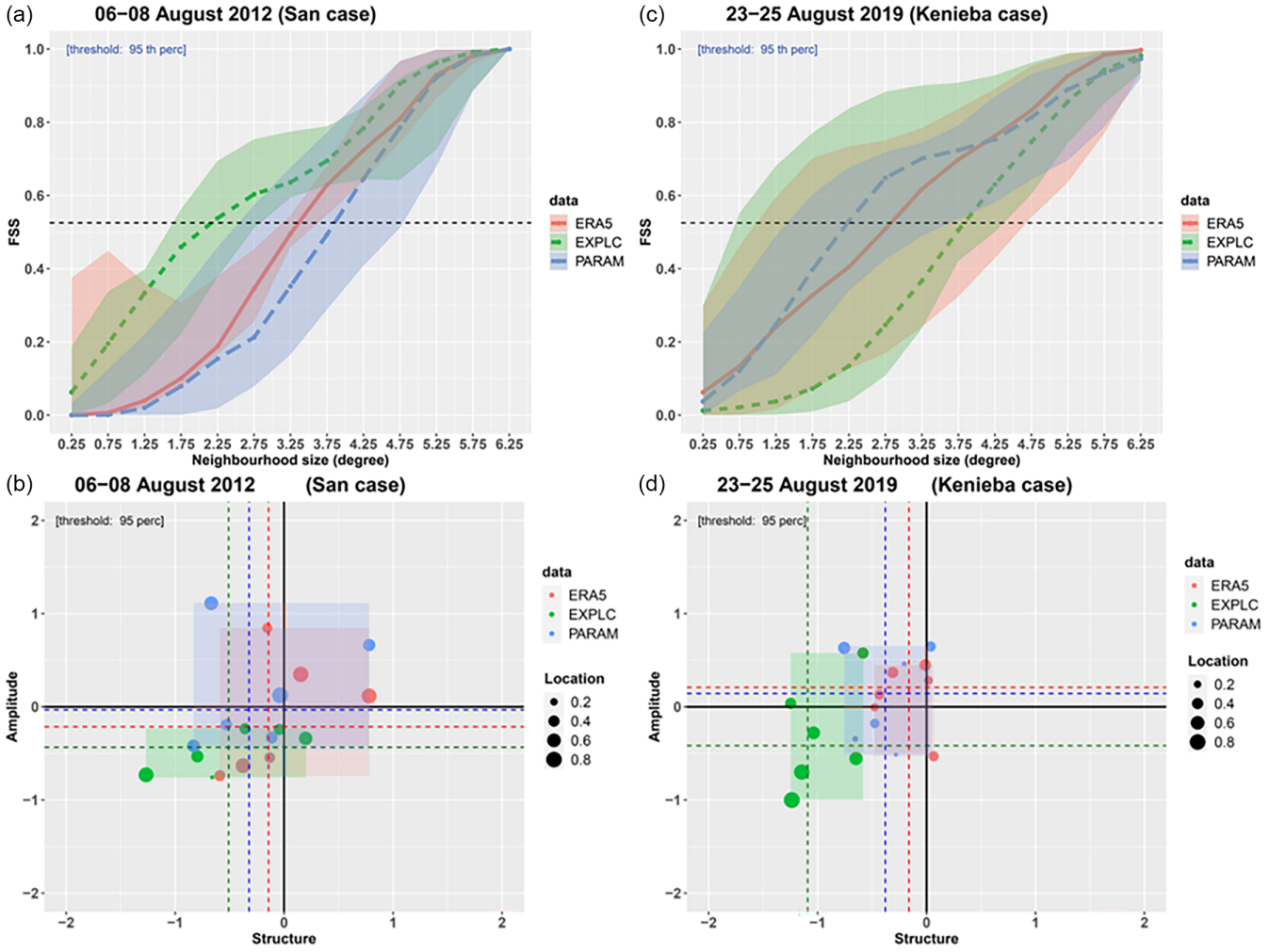


**FIGURE 10** Spatial verification methods (top row) FSS and (bottom row) SAL, applied to (a,b; left column) the San case and (c,d; right column) the Kenieba case with IMERG as the reference. Both FSS and SAL are calculated from the ensemble of timesteps indicated in Figures 3 and 4 for the San and Kenieba cases, respectively. The ensemble of FSS curves (solid lines: median; shaded area: extent of the minimum–maximum) is plotted as a function of neighborhood size (in degrees) for EXPLC, PARAM, and ERA5. The horizontal dashed line denotes $FSS_{\text{uniform}}$. For SAL, the S and A components (structure and amplitude) are represented on the abscissa and ordinate, respectively, while the L component (location) is quantified through the size of the points. The shaded rectangles denote the extent of the minimum–maximum in the S–A component space, while the median is found at the intersection of the dashed lines. The SAL median values for both cases are also indicated in Table 1. [Colour figure can be viewed at wileyonlinelibrary.com]

**TABLE 1** The median values of S, A, and L values from comparing three-hourly rainfall in EXPLC, PARAM, and ERA5 with IMERG for the San and Kenieba cases. The S and A values are additionally represented in Figure 10c,d by dashed lines.

| | San case | | | Kenieba case | | |
|---|---|---|---|---|---|---|
| | **S score** | **A score** | **L score** | **S score** | **A score** | **L score** |
| EXPLC | −0.50 | −0.43 | 0.38 | −1.09 | −0.41 | 0.54 |
| PARAM | −0.32 | −0.03 | 0.44 | −0.37 | −0.14 | 0.22 |
| ERA5 | −0.14 | −0.21 | 0.48 | −0.16 | −0.20 | 0.32 |

### 5.2.2 | Kenieba case

In same fashion as for the San case, Figure 10c,d shows FSS and SAL scores for the Kenieba case considering all 0600 and 1800 UTC timesteps from August 23–25, 2019. As outlined in Section 5.1.2, EXPLC struggles with the organization of convective clusters by producing rather scattered rainfall systems, while PARAM captures the

basic development well. Considering the median FSS, the rainfall fields in PARAM become skillful at a smaller scale than for either EXPLC or ERA5 (intersection of FSS curves with $FSS_{\text{uniform}}$ at 2.25° versus 3° and 3.25°, respectively). However, considering the range of FSS curves, there is a large spread in the performance of EXPLC. Since FSS is a spatial measure, the strong variation of FSS across all timesteps is most likely due to the spatially random nature of unorganized convection. In contrast, the FSS curves of PARAM exhibit much lower variance along the axis of the neighborhood size, which is likely a result of the greater convective organization of the precipitation field compared with EXPLC (cf. Figure 9f).

The SAL method in Figure 10d indicates further the challenges of EXPLC in organizing convection. Among all products, EXPLC shows the largest errors regarding the S component (see also Table 1). In general, the data points are largely concentrated in the bottom-left quadrant, indicating that EXPLC systematically produces too small and too weak rainfall systems. The data points for both PARAM and ERA5 are located closer to the center, thus suggesting smaller amplitude and structural errors in the rainfall fields than for EXPLC. Furthermore, between PARAM and EXPLC, PARAM evidently shows considerably smaller L values, which generally supports the results with FSS in Figure 10c.

Overall, the spatial verification demonstrates that the notion of using EXPLC over PARAM to improve the forecast of extreme precipitation in West Africa is strongly case-dependent. As explored in Section 4.3, the moisture conditions are one major aspect where both cases differ considerably. The next section delves into the performance of ICON in reproducing the dynamical fields, in order to explore the contrasting performance of EXPLC.

## 5.3 | Comparison of dynamical fields between ERA5 and ICON simulations

### 5.3.1 | Wind field

Both the San and Kenieba cases have shown the relevance of a cyclonic vortex in the respective development of extreme rainfall, the latter of which imposed challenges for ICON in capturing it (see Figure 9). To investigate the dynamics associated with the cyclonic vortices, Hovmöller diagrams in Figure 11 depict the evolution of the meridional wind (shading), 700-hPa relative vorticity (solid contours), and 950–600 hPa wind shear (dotted contours) based on ERA5 (Figure 11a,b) and the outputs of EXPLC (Figure 11c,d) and PARAM (Figure 11e,f) for both San (left column) and Kenieba (right column) cases. The variables are averaged over a 5° latitude band centered around the locations of San and Kenieba, respectively.

In general, a slanted dipole in meridional wind in the Hovmöller diagram, in addition to a streak of positive vorticity in its center, usually reflects the propagation of a vortex, which becomes apparent in both cases. For the San case, first signs of an established cyclonic circulation appear around August 5 at 15°E (Figure 11a), which coincides with the longitude of Lake Chad (cf. Figure 5a). From there, the vortex gradually intensifies, as indicated by the strengthening in the meridional wind field, and propagates westwards at a speed of around 9 $m \cdot s^{-1}$, which falls into the typical velocity range of AEWs (Fink & Reiner, 2003; Reed *et al.*, 1977). Upon intensification, the vortex creates a zone of pronounced vertical wind shear (i.e., > 16 $m \cdot s^{-1}$) at its western flank (i.e. within the region of northerlies) at around August 7, which likely facilitated the intensification and organization of the squall line (cf. Figure 9a). Compared with ERA5, clear indications of a stable cyclonic circulation appear later in time in both EXPLC (Figure 11c) and PARAM (Figure 11e), exhibiting a slightly lower propagation velocity (7–8 $m \cdot s^{-1}$) than in ERA5. Moreover, both simulations are unable to produce a comparable area of strong vertical wind shear, which might partly explain the smaller degree of convective organization compared with IMERG. Nonetheless, the overall evolution of the strength of the vortex is captured reasonably in EXPLC, even though the structures in relative vorticity are noisier compared with both PARAM and ERA5. The noisier pattern is likely related to rainfall systems at smaller scales, due to the explicit treatment of convection.

For the Kenieba case, the intensification of the cyclonic vortex, the velocity of which is overall comparable with AEWs as well, sets in roughly one day prior to the event in the evening of August 23 (Figure 11d), concurrent with the convective organization of the rainfall systems (cf. Figure 9b). While PARAM appears to capture the overall structure of the meridional wind field, wind shear, and relative vorticity features reasonably well in space and time (Figure 11f), EXPLC struggles to realize a pronounced vortex towards the event (Figure 11e). Again, the noise in relative vorticity in EXPLC is likely linked to scattered convective cells, which never develop into an organized system over Kenieba (cf. Figure 9d). Eventually, the overproduction of small-scale rainfall features in EXPLC might have inhibited the efficient co-existence of organized convection and vortex.

### 5.3.2 | Moisture field

The Hovmöller diagrams in Figure 12 depict the spatio-temporal evolution of total precipitable water (TPW)

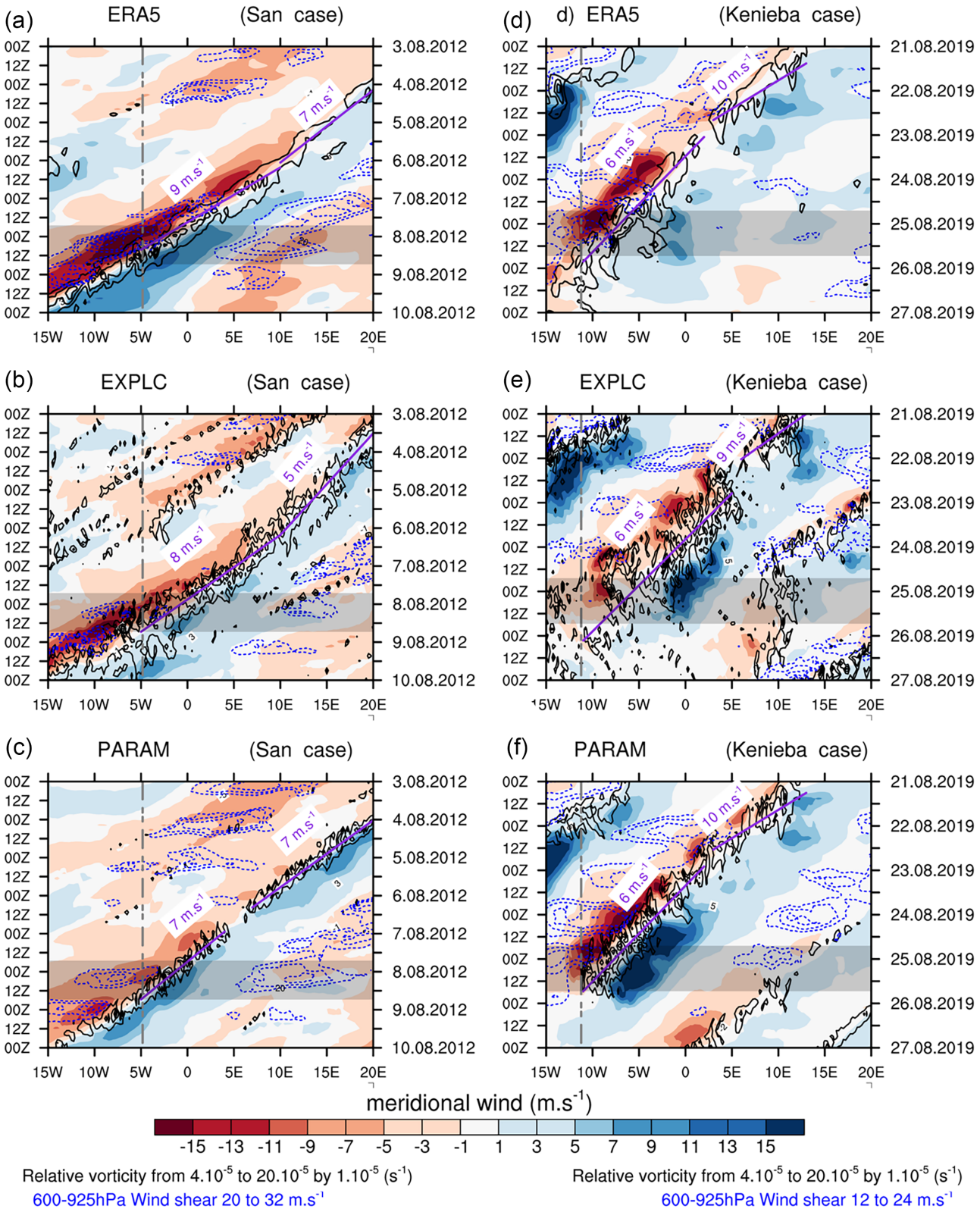


**FIGURE 11** Hovmöller diagrams showing the evolution of 700-hPa relative vorticity (solid contour), 700-hPa meridional wind (shaded), and 925–600 hPa wind shear (dotted contour) from (a, d) ERA5 fields, (b, e) EXPLC, and (c, f) PARAM. The variables are averaged over a 5° latitude band centered around the coordinates of San and Kenieba, respectively. Solid lines indicate the position of maximum vorticity, with the westward propagation velocity labeled. The panels on the left side depict the event of August 8, 2012 in San and panels on the right side the event of August 25, 2019 in Kenieba. The vertical lines indicate the longitudinal positions of San and Kenieba. The horizontal shaded band refers to the time when the rainfall event was active according to IMERG. [Colour figure can be viewed at wileyonlinelibrary.com]

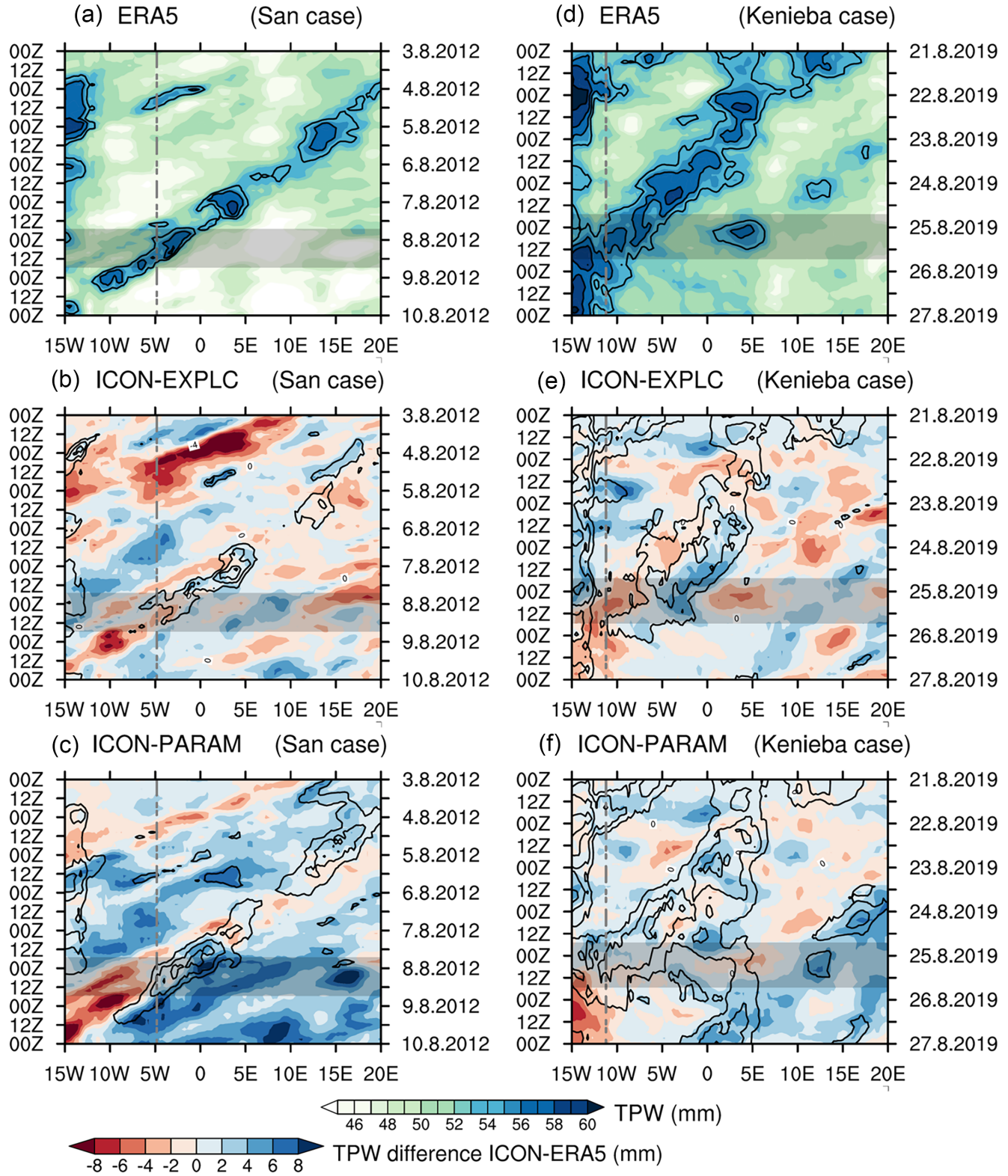


**FIGURE 12** Hovmöller diagrams showing (a,d) the propagation of total precipitable water (TPW) patterns from ERA5, and differences in TPW between (b,e) EXPLC and ERA5 and (c,f) PARAM and ERA5. The variables are averaged over a 5° latitude band centered around the coordinates of San and Kenieba, respectively. The contours show TPW values above 54 mm in 2-mm intervals. The panels on the left side depict the event of August 8, 2012 in San and the panels on the right side the event of August 25, 2019 in Kenieba. The vertical lines indicate the longitudinal positions of San and Kenieba. The horizontal shaded band refers to the time when the rainfall event was active according to IMERG. [Colour figure can be viewed at wileyonlinelibrary.com]

during the two extreme events in EXPLC and PARAM in comparison with ERA5. In both cases, enhanced tropospheric moisture content is clearly related to the respective westward-moving cyclonic vortex (Figure 12a,b). It is also evident that the conditions across West Africa during the Kenieba case are overall moister than during the San case; the reasons for this were outlined and analyzed in Sections 4.3.1 and 4.3.2.

In the San case, EXPLC struggles to concentrate moisture within the vortex to the same level as ERA5 (Figure 12b), which might explain the underestimation in rainfall compared with IMERG (cf. Figure 9c). In this regard, PARAM performs better but exhibits larger deviations in the overall moisture field (Figure 12c). In particular, the drying in the ridge before and after the AEW passage at San is strongly underestimated. The vortices in PARAM and ERA5 are slightly out of phase due to different propagation velocities (see Section 5.3.1), which largely explains the distinct westward-propagating negative anomaly. In the Kenieba case, pronounced differences between EXPLC and PARAM are not as evident as in the San case. Again, PARAM tends to overestimate the moisture content in the area of and beyond the vortex (Figure 12f), whereas EXPLC is largely on the drier side (Figure 12d). Although it is difficult to draw general conclusions about model behavior from two cases alone, PARAM converts the abundance of moisture efficiently into strong precipitation within the vortex. For EXPLC, the Kenieba case hints at issues in moisture-laden conditions, where the explicit treatment of convection in ICON produces too many small-scale rainfall systems too fast. This potential deficiency might be mitigated in situations like the San case, which involves drier airmasses for convective enhancement.

## 6 | SUMMARY AND CONCLUSION

Two extreme rainfall events in Mali during the peak monsoon season, namely the San case around August 8, 2012 and the Kenieba case around August 25, 2019, were investigated with respect to their rainfall structures and dynamical forcings, as well as the ability of DWD's ICON model to represent their evolution. With rainfall amounts of 127 and 126 mm, respectively, in 24 hours, these two cases feature different dynamic drivers that led to the intense rainfall. The daily precipitation accumulations are extreme (i.e., around or above the 99th percentile) in the respective station climatologies, the satellite-based IMERG dataset (final run, V6), and reanalysis data from ERA5. At a horizontal resolution of 6.5 km, ICON was used to perform two sets of simulations for each case: EXPLC and PARAM (ICON without and with convective parameterization, respectively), in order to test the capabilities of the two configurations to represent the extreme rainfall. Using a similar model setup, these experiments were motivated by the study of Pante and Knippertz (2019), who showed that EXPLC configurations generally exhibit a superior representation of Sahelian convection compared with PARAM. IMERG and ERA5 data were used to (a) analyze the extreme precipitation events from a dynamical point of view and (b) evaluate the performance of the model simulations. The most important results are the following.

- The two extreme events at San and Kenieba were caused by organized convection associated with a low-level cyclonic vortex; however, each within different environmental settings. While both cases featured an African easterly wave (AEW), the San case involved convective enhancement along dry Saharan airmasses, whereas the Kenieba case occurred within an unusual widespread wet environment extending deep into the Sahel.
- While EXPLC simulates the San case satisfactorily, PARAM is superior for the Kenieba case. EXPLC exhibits a better representation of AEW-related dynamics and rainfall in the San case—albeit underestimating the overall rainfall amount—but struggles with appropriate convective organization within the anomalously moist environment in the Kenieba case by producing too many scattered rainfall systems. Here, PARAM appears to be capable of converting the abundant moisture into excessive rainfall in a more efficient manner through the moist vortex. This indicates that the alleged benefit of using explicit convection schemes does not always materialize in extreme rainfall cases in the Sahel—at least with ICON.
- The spatial verification of the rainfall fields in ICON with the FSS confirmed the issues of EXPLC in the Kenieba case, which is skillful at larger spatial scales compared with PARAM around the time of the extreme events. Even the grid-scale precipitation fields in ERA5 exhibit more skill than EXPLC, suggesting that parameterized convection might cope better in moisture-laden situations with relatively weak dynamic triggers.
- The analysis with SAL confirms the negative bias in the size and amplitude (i.e., intensity) of precipitation objects in EXPLC for both cases. The fact that EXPLC struggles with convective organization and instead triggers randomly distributed smaller convective cells leads to large location errors, particularly in the Kenieba case. PARAM does not seem to suffer from such deficiencies as soon as the vortex creates large moisture content.

- The two cases were influenced by the presence of convectively favorable phases of both TD/AEW and MRG, that is, fast equatorial wave modes. When overlapping, convective activity and intensity encountered a boost. Furthermore, the AEW during the San case belongs to the 10% most intense in the 20-year August sample (2000–2019). ER, as a slow wave mode, likely had a low impact on the convective activity itself, but might have contributed to the moist conditions during the Kenieba case. These results are consistent with Peyrillé *et al.* (2023).

While EXPLC led to an improved representation of the diurnal cycle of precipitation and the westward propagation of rainfall systems in the Sahel across a large sample of ICON simulations (e.g., Pante & Knippertz, 2019), its performance compared with PARAM can still be highly case-dependent, as the present study suggests. It highlights the potential challenges of EXPLC in forming organized convection in situations with high low-tropospheric moisture content and weak dynamical triggers. Further test simulations with increased spatial resolutions, later initialization times closer to the extreme event, and a different dataset for initial and boundary conditions (i.e., ICON analyses) led to enhanced rainfall amounts, but did not improve the lack of convective organization in ICON substantially for the Kenieba case (not shown).

In this regard, one aspect that has not been addressed directly in this study is the influence of soil moisture on the mesoscale dynamics of convection. Klein and Taylor (2020) have shown that enhanced (zonally oriented) soil moisture gradients as a consequence of a southward excursion of the ITD can generate convective instability by promoting moisture convergence and stronger mesoscale heat fluxes in the planetary boundary layer (PBL). While distinct soil moisture gradients prevailed in the San case, they were considerably less pronounced in the overall moist Kenieba case (not shown). The sensitivity of such different levels of soil moisture variability on the PBL and cloud development in ICON was studied extensively in Han *et al.* (2019) in largely idealized settings. In their large-eddy simulations, the authors found a tendency for more air parcels with high vertical velocities in the case of strongly heterogeneous (cf. San case) soil moisture fields compared with more homogeneous (cf. Kenieba case) fields, thus suggesting higher chances for intense deep convection to form. How this finding in ICON translates into "real-world" NWP scenarios like the present two case studies, especially with respect to convective organization, needs further in-depth exploration to potentially gain more insight into the behavior of EXPLC.

Certainly, results for the San case in this study align with previous studies over West Africa (Bechtold, 2021; Peters *et al.*, 2019), showing good performance of the convection-permitting configuration in simulating the westward-propagating MCSs linked with a pronounced AEW. However, the Kenieba case is one example that stands in contrast to this consensus. Beyond the challenges highlighted for the Sahel, this result may also be of relevance for the densely populated Guinea Coast region, where moisture exists in abundance. Extreme rainfall events in this region involving a moist vortex and high flood risks are increasingly documented, as shown by the works of for example, Maranan *et al.* (2019), (Vondou et al. (2025); submitted to Quart. J. Roy. Met. Soc.), and thus stress the need for reliable forecasts.

Despite the limitations of the study (only one model used and for only two cases), the results open up study perspectives on the following questions. To what extent is EXPLC more suitable for AEW-related extreme precipitation? Is the ability of convective organization in EXPLC generally decreased in situations with widespread high tropospheric moisture load and weak dynamical triggers that lead to many isolated cells? The latter question can be critical, in so far as comparable extreme events such as that in Ouagadougou in 2009 were likely preceded by an unusual Sahelian wet spell as well (Beucher *et al.*, 2020; Lafore *et al.*, 2017). Overall, this study underlines the ongoing need for process-based evaluations of NWP models for the under-studied West Africa region to increase the body of knowledge about atmospheric drivers of intense rainfall, and to identify and improve on continuous shortcomings in the formulation of parameterizations and the overall behavior of models with respect to (extreme) precipitation. Due to the complexity of the dynamics of the West African monsoon, the latter likely requires steps towards more stratified and targeted verification strategies: for example, based on climate zones or dynamical features which carry predictive skill in forecasting rainfall, such as AEWs.

## ACKNOWLEDGEMENTS

This work was supported by the DAAD Climate Research Alumni and Postdocs in Africa—(climapAfrica) Programme. The International Science Programme (ISP/IPPS) through the "Laboratoire d'Optique de Spectroscopie et des Sciences de l'Atmosphère (LOSSA)" at the Faculty of Sciences and Technology is acknowledged for providing workspace and facilities to S. Sanogo during the postdoctoral period. Special thanks to the IMKTRO research group for hosting S. Sanogo during his stay at KIT. We thank Dr Athul Rasheeda Satheesh of IMKTRO for providing Figures 7 and 8. This research was partly

supported by the Deutsche Forschungsgemeinschaft (grant no. SFB/TRR 165, "Waves to Weather") and conducted within the subproject C2: "Statistical-dynamical forecasts of tropical rainfall". A. H. Fink and M. Maranan acknowledge funding from the German Federal Ministry of Education and Research (BMBF) through the WASCAL Research Action Plan 2.0 (WRAP2.0) for FURIFLOOD project (Current and future risks of urban and rural flooding in West Africa—An integrated analysis and eco-system-based solutions; grant No. 01LG2086A) and also from the BMBF project NetCDA (German Academic Network for Capacity Development in Climate Change Adaptations in Africa; grant No. 01LG2301E). Open Access funding enabled and organized by Projekt DEAL.

## FUNDING INFORMATION

This work was supported by the German Federal Ministry of Education and Research (BMBF) through the WASCAL Research Action Plan 2.0 (WRAP2.0) for FURIFLOOD project (Current and future risks of urban and rural flooding in West Africa—An integrated analysis and eco-system-based solutions; grant No. 01LG2086A) and also from the BMBF project NetCDA (German Academic Network for Capacity Development in Climate Change Adaptations in Africa; grant No. 01LG2301E). It was also part of the Deutsche Forschungsgemeinschaft (grant no. SFB/TRR 165, "Waves to Weather") and conducted within the subproject C2: "Statistical-dynamical forecasts of tropical rainfall". The first author, Souleymane Sanogo, was funded by the DAAD Climate Research Alumni and Postdocs in Africa (climapAfrica) Programme.

## CONFLICT OF INTEREST STATEMENT

The authors declare that they have no conflict of interest.

## DATA AVAILABILITY STATEMENT

Station rainfall data used in this article were obtained from the Karlsruhe African Surface Station-Database (KASS-D) from the Institute of Meteorology and Climate Research of the Karlsruhe Institute of Technology, Germany, and from the Mali national agency for Meteorology (Mali-METEO). The ERA5 data were obtained from the Copernicus Climate Change Service (C3S) Climate Data Store (https://cds.climate.copernicus.eu). IMERG data are available through the NASA Earth data portal (https://disc.gsfc.nasa.gov/datasets/GPM_3IMERGHH_06/ and https://disc.gsfc.nasa.gov/datasets/GPM_3IMERGHH_07/).

## ORCID

*Souleymane Sanogo* https://orcid.org/0000-0003-4179-6001
*Marlon Maranan* https://orcid.org/0000-0002-0324-8859
*Andreas H. Fink* https://orcid.org/0000-0002-5840-2120
*Peter Knippertz* https://orcid.org/0000-0001-9856-619X

## REFERENCES

Atiah, W.A., Amekudzi, L.K. & Danuor, S.K. (2023) Mesoscale convective systems and contributions to flood cases in southern west Africa (swa): a systematic review. *Weather and Climate Extremes*, 39, 100551.

Bechtold, P. (2021) Convection and its impact on weather. *Atmosphere*, 12, 437.

Bechtold, P., Köhler, M., Jung, T., Doblas-Reyes, F., Leutbecher, M., Rodwell, M.J. et al. (2008) Advances in simulating atmospheric variability with the ecmwf model: from synoptic to decadal time-scales. *Quarterly Journal of the Royal Meteorological Society: A Journal of the Atmospheric Sciences, Applied Meteorology and Physical Oceanography*, 134, 1337–1351.

Berthou, S., Kendon, E., Rowell, D., Roberts, M., Tucker, S. & Stratton, R. (2019) Larger future intensification of rainfall in the west african sahel in a convection-permitting model. *Geophysical Research Letters*, 46, 13299–13307.

Beucher, F., Lafore, J.-P. & Chapelon, N. (2020) Simulation and analysis of the moist vortex associated with the extreme rain event of ouagadougou in 2009. *Quarterly Journal of the Royal Meteorological Society*, 146, 86–104.

Burpee, R.W. (1972) The origin and structure of easterly waves in the lower troposphere of north africa. *Journal of Atmospheric Sciences*, 29, 77–90.

Cheng, Y.-M., Thorncroft, C.D. & Kiladis, G.N. (2019) Two contrasting african easterly wave behaviors. *Journal of the Atmospheric Sciences*, 76, 1753–1768.

Dezfuli, A.K., Ichoku, C.M., Huffman, G.J., Mohr, K.I., Selker, J.S., Van De Giesen, N. et al. (2017) Validation of imerg precipitation in Africa. *Journal of Hydrometeorology*, 18, 2817–2825.

Diongue, A., Lafore, J.-P., Redelsperger, J.-L. & Roca, R. (2002) Numerical study of a Sahelian synoptic weather system: initiation and mature stages of convection and its interactions with the large-scale dynamics. *Quarterly Journal of the Royal Meteorological Society: A Journal of the Atmospheric Sciences, Applied Meteorology and Physical Oceanography*, 128, 1899–1927.

Douglas, I., Alam, K., Maghenda, M., Mcdonnell, Y., McLean, L. & Campbell, J. (2008) Unjust waters: climate change, flooding and the urban poor in Africa. *Environment and Urbanization*, 20, 187–205.

Engel, T., Fink, A.H., Knippertz, P., Pante, G. & Bliefernicht, J. (2017) Extreme precipitation in the west African cities of Dakar and Ouagadougou: atmospheric dynamics and implications for flood risk assessments. *Journal of Hydrometeorology*, 18, 2937–2957.

Essor. (2012) *Inondations en 4è région: Beaucoup de villages affectes.* https://maliactu.net/inondations-en-4e-region-beaucoup-de-villages-affectes/

Fall, M., Dieng, A.L., Sall, S.M., Sane, Y. & Diakhaté, M. (2020) Synoptic analysis of extreme rainfall event in west Africa: the case of Linguère. *American Journal of Environmental Protection*, 8, 1–9.

Fink, A., Vincent, D. & Ermert, V. (2006) Rainfall types in the west African Sudanian zone during the summer monsoon 2002. *Monthly Weather Review*, 134, 2143–2164.

Fink, A.H. & Reiner, A. (2003) Spatiotemporal variability of the relation between African easterly waves and west African squall lines in 1998 and 1999. *Journal of Geophysical Research: Atmospheres*, 108, 4332. https://doi.org/10.1029/2002JD002816

Fink, A.H., Engel, T., Ermert, V., van der Linden, R., Schneidewind, M., Redl, R. et al. (2017) Mean climate and seasonal cycle. In: Parker D. J. & Diop-Kane, M. (Eds.) *Meteorology of tropical West Africa: the forecasters' handbook*, Hoboken, NJ: John Wiley & Sons, pp. 1–39.

Gosset, M., Alcoba, M., Roca, R., Cloché, S. & Urbani, G. (2018) Evaluation of Tapeer daily estimates and other GPM-era products against dense gauge networks in west Africa, analysing ground reference uncertainty. *Quarterly Journal of the Royal Meteorological Society*, 144, 255–269.

Guichard, F., Asencio, N., Peugeot, C., Bock, O., Redelsperger, J.-L., Cui, X. et al. (2010) An intercomparison of simulated rainfall and evapotranspiration associated with a mesoscale convective system over west africa. *Weather and Forecasting*, 25, 37–60.

Han, C., Brdar, S. & Kollet, S. (2019) Response of convective boundary layer and shallow cumulus to soil moisture heterogeneity: a large-eddy simulation study. *Journal of Advances in Modeling Earth Systems*, 11, 4305–4322.

Hersbach, H., Bell, B., Berrisford, P., Hirahara, S., Horányi, A., Muñoz-Sabater, J. et al. (2020) The era5 global reanalysis. *Quarterly Journal of the Royal Meteorological Society*, 146, 1999–2049.

Huffman, G.J., Bolvin, D.T., Braithwaite, D., Hsu, K., Joyce, R., Xie, P. et al. (2015) Nasa global precipitation measurement (gpm) integrated multi-satellite retrievals for gpm (imerg). *Algorithm Theoretical Basis Document (ATBD) Version*, 4.

Huffman, G.J., Bolvin, D.T., Nelkin, E.J., Stocker, E.F. & Tan, J. (2019) *V06 imerg release notes*. NASA/GSFC. Greenbelt, MD. https://gpm.nasa.gov/sites/default/files/2020-10/IMERG_V06_release_notes_201006_0.pdf

Huffman, G.J., Bolvin, D.T., Nelkin, E.J., Wolff, D.B., Adler, R.F., Gu, G. et al. (2007) The trmm multisatellite precipitation analysis (TMPA): quasi-global, multiyear, combined-sensor precipitation estimates at fine scales. *Journal of Hydrometeorology*, 8, 38–55.

IFRC. (2019) *Mali: Floods - emergency plan of action (epoa) dref no. mdrml014 / pml028*. https://reliefweb.int/report/mali/mali-floods-emergency-plan-action-epoa-dref-n-mdrml014-pml028

Janiga, M.A. & Thorncroft, C.D. (2014) Convection over tropical Africa and the east Atlantic during the west African monsoon: regional and diurnal variability. *Journal of Climate*, 27, 4159–4188.

Jiang, Q., Li, W., Fan, Z., He, X., Sun, W., Chen, S. et al. (2021) Evaluation of the era5 reanalysis precipitation dataset over Chinese mainland. *Journal of Hydrology*, 595, 125660.

Johnson, Z.F. & Hitchens, N.M. (2018) Effects of soil moisture on the longitudinal dryline position in the southern great plains. *Journal of Hydrometeorology*, 19, 273–287.

Judt, F. (2020) Atmospheric predictability of the tropics, middle latitudes, and polar regions explored through global storm-resolving simulations. *Journal of the Atmospheric Sciences*, 77, 257–276.

Kendon, E.J., Stratton, R.A., Tucker, S., Marsham, J.H., Berthou, S., Rowell, D.P. et al. (2019) Enhanced future changes in wet and dry extremes over Africa at convection-permitting scale. *Nature Communications*, 10, 1794.

Klein, C. & Taylor, C.M. (2020) Dry soils can intensify mesoscale convective systems. *Proceedings of the National Academy of Sciences*, 117, 21132–21137.

Knippertz, P. & Fink, A.H. (2008) Dry-season precipitation in tropical west Africa and its relation to forcing from the extratropics. *Monthly Weather Review*, 136, 3579–3596.

Knippertz, P. & Martin, J.E. (2005) Tropical plumes and extreme precipitation in subtropical and tropical west Africa. *Quarterly Journal of the Royal Meteorological Society*, 131, 2337–2365.

Knippertz, P., Fink, A.H., Deroubaix, A., Morris, E., Tocquer, F., Evans, M.J. et al. (2017) A meteorological and chemical overview of the DACCIWA field campaign in west Africa in June–July 2016. *Atmospheric Chemistry and Physics*, 17, 10893–10918.

Knippertz, P., Gehne, M., Kiladis, G.N., Kikuchi, K., Rasheeda Satheesh, A., Roundy, P.E. et al. (2022) The intricacies of identifying equatorial waves. *Quarterly Journal of the Royal Meteorological Society*, 148, 2814–2852.

Lafore, J.-P., Beucher, F., Peyrillé, P., Diongue-Niang, A., Chapelon, N., Bouniol, D. et al. (2017) A multi-scale analysis of the extreme rain event of ouagadougou in 2009. *Quarterly Journal of the Royal Meteorological Society*, 143, 3094–3109.

Lavaysse, C., Flamant, C., Janicot, S., Parker, D.J., Lafore, J.-P., Sultan, B. et al. (2009) Seasonal evolution of the west African heat low: a climatological perspective. *Climate Dynamics*, 33, 313–330.

Lavers, D.A., Simmons, A., Vamborg, F. & Rodwell, M.J. (2022) An evaluation of era5 precipitation for climate monitoring. *Quarterly Journal of the Royal Meteorological Society*, 148, 3152–3165.

Liu, Z. (2016) Comparison of integrated multisatellite retrievals for GPM (imerg) and TRMM multisatellite precipitation analysis (TMPA) monthly precipitation products: initial results. *Journal of Hydrometeorology*, 17, 777–790.

Maranan, M., Fink, A.H. & Knippertz, P. (2018) Rainfall types over southern west Africa: objective identification, climatology and synoptic environment. *Quarterly Journal of the Royal Meteorological Society*, 144, 1628–1648.

Maranan, M., Fink, A.H., Knippertz, P., Amekudzi, L.K., Atiah, W.A. & Stengel, M. (2020) A process-based validation of GPM imerg and its sources using a mesoscale rain gauge network in the west African forest zone. *Journal of Hydrometeorology*, 21, 729–749.

Maranan, M., Fink, A.H., Knippertz, P., Francis, S.D., Akpo, A.B., Jegede, G. et al. (2019) Interactions between convection and a moist vortex associated with an extreme rainfall event over southern west Africa. *Monthly Weather Review*, 147, 2309–2328.

Matsuno, T. (1966) Quasi-geostrophic motions in the equatorial area. *Journal of the Meteorological Society of Japan. Series. II*, 44, 25–43.

Murphy, A.H. & Epstein, E.S. (1989) Skill scores and correlation coefficients in model verification. *Monthly Weather Review*, 117, 572–582.

Nicholson, S.E., Fink, A.H., Funk, C., Klotter, D.A. & Satheesh, A.R. (2022) Meteorological causes of the catastrophic rains of October/November 2019 in equatorial Africa. *Global and Planetary Change*, 208, 103687.

Nicholson, S.E., Funk, C. & Fink, A.H. (2018) Rainfall over the African continent from the 19th through the 21st century. *Global and Planetary Change*, 165, 114–127.

Njau, L. & Thiaw, W. (2011) Western Africa [in "state of the climate in 2010"]. *Bulletin of the American Meteorological Society*, 92, S193–S194.

OCHA. (2012) *Ocha situation report – mali complex emergency*. https://reliefweb.int/sites/reliefweb.int/files/resources/full

OCHA. (2017) *West and central Africa: 2017 flood impact*. https://reliefweb.int/sites/reliefweb.int/files/resources/OCHA-ROWCA

Paeth, H., Fink, A.H., Pohle, S., Keis, F., Mächel, H. & Samimi, C. (2011) Meteorological characteristics and potential causes of the 2007 flood in Sub-Saharan Africa. *International Journal of Climatology*, 31, 1908–1926.

Pante, G. & Knippertz, P. (2019) Resolving Sahelian thunderstorms improves mid-latitude weather forecasts. *Nature Communications*, 10, 1–9.

Panthou, G., Vischel, T. & Lebel, T. (2014) Recent trends in the regime of extreme rainfall in the central Sahel. *International Journal of Climatology*, 34, 3998–4006.

Peters, K., Hohenegger, C. & Klocke, D. (2019) Different representation of mesoscale convective systems in convection-permitting and convection-parameterizing NWP models and its implications for large-scale forecast evolution. *Atmosphere*, 10, 503.

Peyrillé, P., Roehrig, R. & Sanogo, S. (2023) Tropical waves are key drivers of extreme precipitation events in the central sahel. *Geophysical Research Letters*, 50, e2023GL103715.

Pocernich, M. (2015) *Package verification. CRAN. R-project. org Internet, 2013–07*.

Raji, K., Ogunjobi, K. & Akinsanola, A. (2017) Radiative effects of dust aerosol on west African climate using simulations from regcm4. *Modeling Earth Systems and Environment*, 3, 1–24.

Rasheeda Satheesh, A., Knippertz, P. & Fink, A.H. (2025) Machine learning models for daily rainfall forecasting in northern tropical Africa using tropical wave predictors. *Weather and Forecasting*, 40, 1895–1916.

Redelsperger, J.-L., Diongue, A., Diedhiou, A., Ceron, J.-P., Diop, M., Gueremy, J.-F. et al. (2002) Multi-scale description of a Sahelian synoptic weather system representative of the west African monsoon. *Quarterly Journal of the Royal Meteorological Society: A Journal of the Atmospheric Sciences, Applied Meteorology and Physical Oceanography*, 128, 1229–1257.

Reed, R.J., Norquist, D.C. & Recker, E.E. (1977) The structure and properties of African wave disturbances as observed during phase iii of gate. *Monthly Weather Review*, 105, 317–333.

Reinert, D., Prill, F., Frank, H., Denhard, M. & Zängl, G. (2018) *Database reference manual for icon and icon-eps (version 1.2. 2)*.

Riley, E.M., Mapes, B.E. & Tulich, S.N. (2011) Clouds associated with the madden–Julian oscillation: a new perspective from cloudsat. *Journal of the Atmospheric Sciences*, 68, 3032–3051.

Rivoire, P., Martius, O. & Naveau, P. (2021) A comparison of moderate and extreme era-5 daily precipitation with two observational data sets. *Earth and Space Science*, 8, e2020EA001633.

Roberts, N. (2008) Assessing the spatial and temporal variation in the skill of precipitation forecasts from an NWP model. *Meteorological Applications*, 15, 163–169.

Roberts, N.M. & Lean, H.W. (2008) Scale-selective verification of rainfall accumulations from high-resolution forecasts of convective events. *Monthly Weather Review*, 136, 78–97.

Roundy, P.E. (2018) A wave-number frequency wavelet analysis of convectively coupled equatorial waves and the MJO over the Indian ocean. *Quarterly Journal of the Royal Meteorological Society*, 144, 333–343.

Rubin, S., Ziv, B. & Paldor, N. (2007) Tropical plumes over eastern north Africa as a source of rain in the middle east. *Monthly Weather Review*, 135, 4135–4148.

Sanogo, S., Fink, A.H., Omotosho, J.A., Ba, A., Redl, R. & Ermert, V. (2015) Spatio-temporal characteristics of the recent rainfall recovery in west Africa. *International Journal of Climatology*, 35, 4589–4605.

Schlueter, A., Fink, A.H. & Knippertz, P. (2019a) A systematic comparison of tropical waves over northern Africa. Part II: dynamics and thermodynamics. *Journal of Climate*, 32, 2605–2625.

Schlueter, A., Fink, A.H., Knippertz, P. & Vogel, P. (2019b) A systematic comparison of tropical waves over northern Africa. Part I: influence on rainfall. *Journal of Climate*, 32, 1501–1523.

Seregina, L.S., Fink, A.H., van der Linden, R., Elagib, N.A. & Pinto, J.G. (2019) A new and flexible rainy season definition: validation for the greater horn of Africa and application to rainfall trends. *International Journal of Climatology*, 39, 989–1012.

Sima, F., Kamga, A., Raiva, I., Dekaa, S. & James, A. (2013) West Africa [in state of the climate in 2012]. *Bulletin of the American Meteorological Society*, 94, S164–S166.

Thorncroft, C.D., Nguyen, H., Zhang, C. & Peyrillé, P. (2011) Annual cycle of the west African monsoon: regional circulations and associated water vapour transport. *Quarterly Journal of the Royal Meteorological Society*, 137, 129–147.

Tiedtke, M. (1989) A comprehensive mass flux scheme for cumulus parameterization in large-scale models. *Monthly Weather Review*, 117, 1779–1800.

Tschakert, P., Sagoe, R., Ofori-Darko, G. & Codjoe, S.N. (2010) Floods in the Sahel: an analysis of anomalies, memory, and anticipatory learning. *Climatic Change*, 103, 471–502.

Vogel, P., Knippertz, P., Fink, A.H., Schlueter, A. & Gneiting, T. (2018) Skill of global raw and postprocessed ensemble predictions of rainfall over northern tropical Africa. *Weather and Forecasting*, 33, 369–388.

Vogel, P., Knippertz, P., Fink, A.H., Schlueter, A. & Gneiting, T. (2020) Skill of global raw and postprocessed ensemble predictions of rainfall in the tropics. *Weather and Forecasting*, 35, 2367–2385.

Vondou, D.A., Maranan, M., Fink, A.H. & Knippertz, P. (2025) Meteorological conditions leading to a catastrophic, rain-induced landslide in Cameroon in October 2019. Quarterly Journal of the Royal Meteorological Society, e70066. https://doi.org/10.1002/qj.70066

Wernli, H., Paulat, M., Hagen, M. & Frei, C. (2008) Sal–a novel quality measure for the verification of quantitative precipitation forecasts. *Monthly Weather Review*, 136, 4470–4487.

Westra, S., Fowler, H.J., Evans, J.P., Alexander, L.V., Berg, P., Johnson, F. et al. (2014) Future changes to the intensity and frequency of short-duration extreme rainfall. *Reviews of Geophysics*, 52, 522–555.

Wheeler, M. & Kiladis, G.N. (1999) Convectively coupled equatorial waves: analysis of clouds and temperature in the wavenumber–frequency domain. *Journal of the Atmospheric Sciences*, 56, 374–399.

Yang, G.-Y., Methven, J., Woolnough, S., Hodges, K. & Hoskins, B. (2018) Linking African easterly wave activity with equatorial waves and the influence of rossby waves from the southern hemisphere. *Journal of the Atmospheric Sciences*, 75, 1783–1809.

Yasunaga, K. & Mapes, B. (2012) Differences between more divergent and more rotational types of convectively coupled equatorial

waves. Part ii: composite analysis based on space–time filtering. *Journal of the Atmospheric Sciences*, 69, 17–34.

Zängl, G., Reinert, D., Rípodas, P. & Baldauf, M. (2015) The icon (icosahedral non-hydrostatic) modelling framework of DWD and MPI-M: description of the non-hydrostatic dynamical core. *Quarterly Journal of the Royal Meteorological Society*, 141, 563–579.

Zipser, E.J., Cecil, D.J., Liu, C., Nesbitt, S.W. & Yorty, D.P. (2006) Where are the most intense thunderstorms on earth? *Bulletin of the American Meteorological Society*, 87, 1057–1072.

**How to cite this article:** Sanogo, S., Maranan, M., Fink, A.H., Woodhams, B.J. & Knippertz, P. (2025) Dynamics and model representation of two contrasting extreme precipitation events in the Sahel. *Quarterly Journal of the Royal Meteorological Society*, e70084. Available from: https://doi.org/10.1002/qj.70084